Experimental investigations on the vortex-shedding from a highly tapered circular cylinder in smooth flow

Stefano Brusco [a,*], Anna Bagnara [b], Stefano Cammelli [c], Giuseppe Piccardo [a]

[a] *Department of Civil, Chemical and Environmental Engineering, DICCA, Polytechnic School, University of Genova, Via Montallegro 1, 16145, Genoa, Italy*
[b] *NOVA Fluid Mechanics, Teddington, London, UK*
[c] *WSP, London, UK*

ARTICLE INFO

ABSTRACT

This paper presents the results of a wind tunnel test campaign conducted to investigate the aeroelastic and aerodynamic behaviour of a tapered circular cylinder in smooth flow conditions. The model under investigation is a single-mode aeroelastic one, whose taper ratio (in terms of diameter) is 8 %. Its global dynamic response was measured through the use of an internally-mounted piezo-electric accelerometer. The sensitivity of the vortex-induced response to different levels of structural damping was explored. The harmonic content of the wake was also measured through a hot-wire anemometer positioned downstream of the wind tunnel model at different heights: this allowed the detection of the portion of the model whose local resonance was accountable for the highest vortex-induced structural response. To further expand the findings of the wake measurements, four 'rings' of surface-mounted pressure sensors were installed on the wind tunnel model. The Reynolds number that was covered during the experiments ranged between 9.3×10^3 and 3.2×10^4.

The experimental investigations revealed that the tapering has a beneficial effect with respect to vortex-induced oscillations, reducing their magnitudes when compared against the ones of a parallel-sided circular cylinder. On the other hand, the lock-in region was found to be wider, exhibiting three distinct peak regions for the lowest level of structural damping. The combined results from the accelerometer, the hot-wire anemometer and the pressure measurements, and the application of tailored time–frequency analyses based on the continuous wavelet transform, revealed that the maximum dynamic response is linked to the local resonance between the fundamental frequency and the bottom portion of the structure. Furthermore, the magnitudes of the local mean aerodynamic drag coefficient and the local standard deviation of the (vortex-induced) lift coefficient were found to be considerably lower than those of a parallel-sided circular cylinder.

1. Introduction

Vortex-induced vibrations (VIVs) caused by wind were known since ancient times and constitute the main component of the crosswind response of slender structures (e.g., Solari, 1985, 2019). The most dangerous situation for a dynamic

* Corresponding author.
   E-mail address: stefano.brusco@edu.unige.it (S. Brusco).

system is represented by the shedding of the vortices tuned to one of the natural frequencies of the structure. Violations of the Strouhal law can occur, causing the lock-in of the shedding frequency over a natural one. The synchronization is maintained within a speed range, above which the tuning vanishes and the Strouhal law is newly valid. The lock-in is favoured when the mass and the damping ratio of the system are low and its insurgence often dominates the serviceability, strength, and fatigue design of slender elements (e.g., Pagnini and Piccardo, 2017).

Research on vortex-shedding response dates back in the 1960s. Extensive wind tunnel testing campaigns, particularly on bridges and stacks (Scruton, 1956, 1963; Scruton and Flint, 1964), took place within the Aerodynamic Division of the National Physical Laboratory in Teddington (UK) under the supervision of Cristopher 'Kit' Scruton. Moreover, Wooton (1969) carried out pioneering wind tunnel tests on models of vertical stacks, which still nowadays represent a reference point in the field, addressing the role of several parameters affecting VIVs. Another important study in this field is represented by the work developed by Feng (1968). Experimental investigations, combined with numerical ones, were vital for the calibration of theoretical models (Sarpkaya, 2004). In particular, the mathematical description offered by the van der Pol model emerged as the most appropriate choice to capture the inherently non-linear and self-governed nature of the phenomenon. The simplification of this type of modelling, with the introduction of an equivalent linear aerodynamic damping, allowed Vickery and Basu (1983) to significantly advance the understanding of the vortex-shedding phenomenon from a technical point of view. Indeed, their semi-empirical model to predict vortex-shedding response of slender structures is able to represent the key features of the lock-in phenomenon. In fact, the dependence of the amplitudes on the "mass-damping parameter" was well-captured (see also Vickery, 1981). Theirs is just one of several mass-damping parameters defined in the literature (all proportional to the product between the damping ratio ξ and the mass ratio $\frac{m_e}{\rho D_{ref}^2}$, where m_e is the equivalent mass of the model, D_{ref} is the reference dimensions in the crosswind direction and ρ is the density of the fluid; see also Williamson and Govarhan, 2004; Vandiver, 2012). A commonly used expression of this parameter is $\frac{4\pi m_e \xi}{\rho D_{ref}^2}$, which was denoted as the Scruton number in the early 1980s (Zdravkovich, 1982).

Contrary to the case of parallel-sided structures, the number of publications dedicated to experimental campaigns on circular tapered structure subsequent to the pioneering works by Scruton (1956, 1963) is quite scarce. In Scruton (1956), the effect of the taper was studied by using sectional models of circular cylinders (whose ratio between the base and the tip diameter is 1.5, and whose taper diameter ratio is close to 3%) indicating that the aerodynamic excitation was at least as vigorous as that for the parallel-sided cylinder. Moreover, the amplitudes of oscillation seem extremely sensitive to small increments of damping ratio, differently from parallel-sided cylinders. Amongst the several tests mentioned in Scruton (1963), there is one pertaining a three-dimensional aeroelastic model of a slender stack, characterized by a considerable degree of taper (almost 4% in terms of diameter). Scruton only partially confirmed what he had found in 1956: for low values of structural damping and smooth flow conditions, the results pointed out the presence of three different regions of amplification of the response, corresponding to local resonances between portions of the model and one of the natural frequencies. At least two distinct diameters were said to govern the structural behaviour: the first one was identified near the top of the stack, while the second one was collocated further down. In both works, the experimental campaigns were conducted at a sufficiently high Reynolds number (Re) range (close to 10^5).

A fundamental contribution to the subject of vortex-shedding for tapered structures was produced by Vickery and Clark (1972). In their experimental investigation, a slender and tapered (4% in terms of diameter) circular structure was tested making use of a 0.914 m tall static pressure and aeroelastic models, in both smooth uniform and turbulent flow, with Re< 10^5. The maximum response in the main structural mode occurs when the shedding frequency near the bottom third of the stack is close to the natural frequency. On the other hand, the presence of regions where the shedding frequency was locked on a fixed value – rather than varying according with a constant local Strouhal number – were detected under smooth flow conditions. This finding confirms the existence of constant-frequency vortex cells (i.e., regions characterized by a constant vortex-shedding frequency with transition zones in between) in the wake of tapered cylinders, which is consistent with what documented in a number of references from the wider fluid dynamics literature, where it is referred as cellular vortex-shedding. In the low Reynolds number regime, papers on this topic are by Gaster (1971), Papangelou (1992) and Piccirillo and Van Atta (1997). For higher Reynolds numbers ($Re \sim 3.6 \times 10^4$), the cellular nature of the vortex-shedding from fixed tapered cylinders has been documented by Balasubramanian et al. (1998), who described the similarity and the possible additivity of the effects of shear flow and taper. Furthermore, Hsiao and Chiang (1998) highlighted the existence of two/three vortex cells, noting that their sizes and numbers appear to be influenced by the Reynolds number (ranging from 1.4×10^3 to 4×10^4), as well as by the taper ratio. To this extent, a tapered circular structure seems to behave similarly to a uniform circular cylinder in shear flow, with a "step-by-step" variation of the shedding frequency along the structure, forming cells of constant frequency (e.g., Maull and Young, 1973; Griffin, 1985; Facchinetti et al., 2002).

The vortical structures forming behind a tapered cylinder are therefore known to be different than those generated from a parallel-sided one under the same flow condition, and so is the relevant wake dynamics, in particular in lock-in regions. As far as parallel-sided cylinders are concerned, several investigations in literature have focused on these aspects (e.g., Williamson and Govarhan, 2004; Sarpkaya, 2004). Specifically, Williamson and Roshko (1988) clarified that the peak of the response is associated with a change in the vortex wake modes, leading to a hysteresis of the response with a switch between the so-called "initial" and "lower" branches of the response (from two single vortices '2S' to two vortex pairs '2P' in one cycle of vortex-shedding). The case of a tapered system seems instead characterized by a "hybrid" shedding
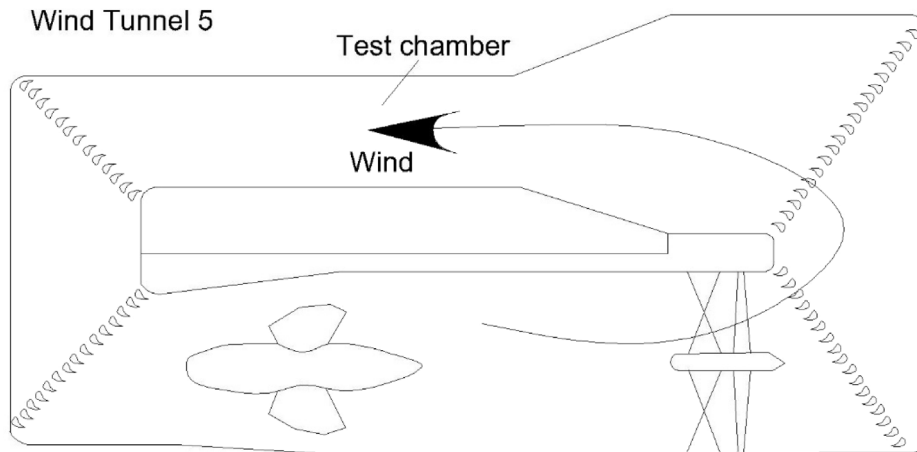
Fig. 1. Outline of WT5.

mode, as proposed by Techet et al. (1998), for which different '2S' and '2P' vortex patterns may coexist along the axis of the model.

A literature review on the dynamic response of tapered structures revealed that this topic is not well developed as it is for parallel-sided structures, especially in the context of civil engineering applications, although some contributions do exist in the offshore engineering (e.g., Zeinoddini et al., 2013; Kaja et al., 2016). Balasubramanian et al. (2001) experimentally studied different configurations of pivoted tapered structures and shear flows. The presence of a tapered structure seems to lead to a wider lock-in range if compared with the corresponding parallel-sided one.

Based on the information provided, it is evident that there is a significant level of uncertainty concerning the taper effect in relation to VIVs. Furthermore, there is currently a lack of solid technical recommendations regarding advantageous configurations to employ. Blevins (2001), by suggesting a taper angle of 8–10 degrees in the downstream side of the structure as an effective measure to mitigate VIVs, is one of the few references that provides some guidelines on this subject.

To shed further light on this matter, this paper presents the outcome of an experimental investigation of a highly tapered circular cylinder (8% in terms of taper diameter, at least double compared to the classic references mentioned above on the circular-shaped cross section), carried out through a wind tunnel test campaign in smooth flow conditions. The objective of this study is to elucidate the effectiveness of a substantial degree of taper in mitigating VIVs, while also establishing a connection between such mitigation and the cellular structure of vortex shedding. The wind tunnel model used in the investigation was initially conceived to be a single-mode aeroelastic model. This was subsequently converted into a pressure model for a second phase of the experimental campaign. The wind tunnel test campaigns, as well as the facility, the models and the relevant instrumentations are described in Section 2. Section 3 presents the main outcomes of the study of the aeroelastic model. Once the model was converted into a rigid one, additional investigations on its aerodynamic behaviour are shown in Section 4. Finally, Section 5 draws the main conclusions of this work.

2. Description of the wind tunnel test campaign

2.1. Experimental facility

The wind tunnel used to carry out the experimental work presented within this paper was the aeronautical wind tunnel facility (Tunnel 5) of what once was the 'Wind Engineering' business unit of BMT Group (now inherited by NOVA Fluid Mechanics) in Teddington (London, UK). Its closed-circuit chamber featured an octagonal test section which was 2.74 m wide and 2.14 m high. The operational wind speed ranged from 0.2 m/s to 65 m/s. The wind speed could be accurately set and held constant in fine increments over the full operating range. The wind speed in the wind tunnel was continuously monitored by using two Pitot static tubes aligned with the flow.

The outline of the wind tunnel airline is indicated in Fig. 1 in schematic form.

Measurements concerning vertical profiles of mean wind speed and turbulence intensity in smooth flow were carried out, whose outcomes are reported in Fig. 2a and b (mean wind velocity and turbulence intensity, respectively). The maximum level of inherent turbulence in that condition above 0.2 m was not larger than 0.3%, i.e. aligned with best industry standard for section model wind tunnel testing.
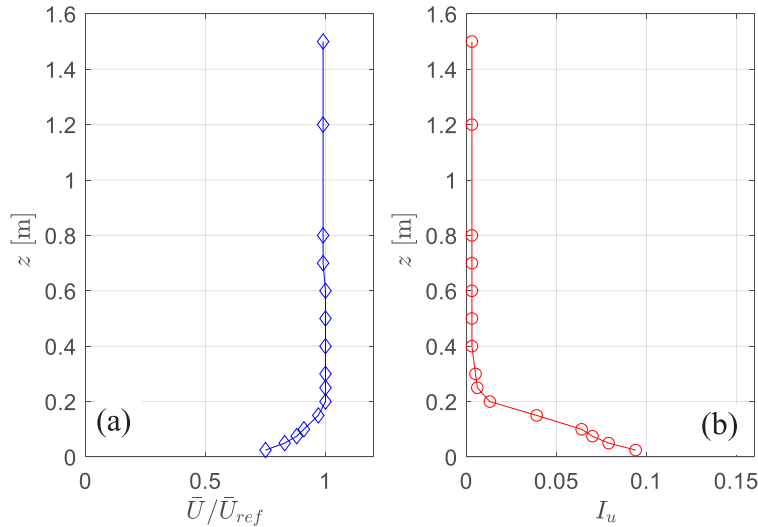
Fig. 2. Vertical profiles measured in Tunnel 5, in smooth flow: (a) mean wind velocity (normalized to the measurement at 1.5 m); (b) turbulence intensity.

2.2. Wind tunnel model and relevant instrumentation

The wind tunnel model was a single-mode model of a tapered circular cylinder. This allowed a good representation of the first order bending modes, as well as the reproduction of the effects linked with taper and tip. The external envelope of the model was manufactured using balsa wood; more precisely, eleven tapered thin-walled truncated cones were connected to a rigid carbon-fibre spine through horizontal balsa stiffeners. The model was 1.5 m tall (L); its diameter was 0.13 m at the base and 0.01 m at the top, leading to a slope of 8% in terms of diameter (Fig. 3). The mean diameter of the entire model was considered as reference throughout the experimental campaign, $D_{ref} = 0.07$ m. The blockage induced by its presence in the wind tunnel was limited (less than 6%). No corrections were applied, albeit blockage effects on slender structures in wind tunnel are still not fully understood and may deserve further studies, especially regarding crosswind effects (e.g., Laneville, 1990). The wind tunnel model was firstly employed as an aeroelastic one (whose structural properties are described in Section 2.2.1), enabling the study of the fluid–structure interaction. Its dynamic response was firstly investigated by means of a purposely designed three-axial internal accelerometer mounted inside the model, in proximity of its tip, precisely at 1.37 m from the base. Secondly, a hot-wire anemometer was installed downstream at different heights, to capture the variation of the harmonic content with height. In a second phase, a portion of the model (close to the base) was instrumented with four rings of pressure sensors (Section 2.2.2), which were key for the definition of the local aerodynamic properties.

2.2.1. Aeroelastic model

The single-mode model was mounted on a gimbal system at its base (Fig. 4a); the required elastic stiffness was provided by an arrangement of helical springs connected at the base of the spine of the model (Fig. 4b).

To study the crosswind response of the structure, the effective direction of the gimbal was chosen to be perpendicularly to the one of the on-coming flow. Furthermore, the model was restrained from moving in the alongwind direction through the presence of a steel wire. The layout of the dynamic rig is shown in Fig. 5a. A raised wood table (Fig. 5a) was included to limit the influence of the boundary layer. Specifically, this was possible through the installation of a wing profile at the upstream side of the table. In this configuration, the tip of the model was almost 0.60 m far from the ceiling, which was noted to be sufficient to avoid boundary layer effects (Figs. 2a and 2b), as well as to limit local effects due to the proximity between structure and wind tunnel walls. The vertical carbon-fibre stick, which connects the model to the elastic and dissipative devices, is effectively shielded by the presence of short profiles positioned beneath the wooden table (Fig. 5a). Fig. 5a also shows the position of the two aforementioned Pitot-static tubes. The reference wind velocity was taken from the upstream one, since its measurement is not affected by the presence of the model itself. A picture of the wind tunnel set-up is shown in Fig. 5b.

As first task of the preliminary tests phase, the modal shape of the structure was estimated. This was possible through the installation of two accelerometers, located on the external envelope of the structure at different heights. In particular, the top one was installed at 1.37 m from the base (consistently with the internal accelerometer mentioned in Section 2.2). The other one was positioned at different heights throughout the vertical axis of the cylinder. The model shape could thus be identified as $\psi_y(z) = \left(\frac{z}{L}\right)^{1.2}$, being z the cylinder axis starting from the base of the model, and y the coordinate in
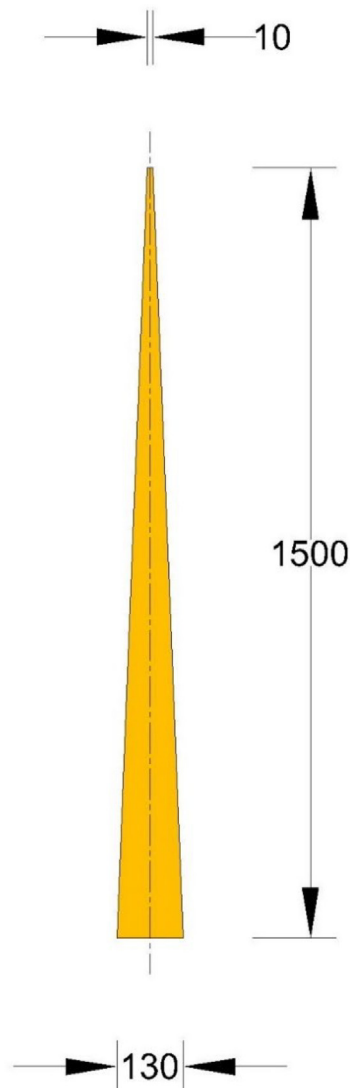
**Fig. 3.** Geometry of the wind tunnel model (dimensions in millimeters).

the crosswind direction. The natural frequency of the wind tunnel model, denoted as n_0, was set to 9.1 Hz, a frequency that is well lower than the inherent bending frequency of the model. Moreover, the equivalent mass per unit length in the crosswind mode, m_{eq}, was estimated as 0.312 kg/m, while the polar inertia was 0.488 Kg·m². Dynamic tests were conducted for a single wind direction, due to the polar-symmetry of the system, and for one configuration in terms of stiffness and mass.

When required, additional structural damping was provided through an eddy current damping system (Fig. 4b). This acted on the copper plate attached at the bottom end of the spine of the wind tunnel model (Fig. 4b), hence allowing damping sensitivity studies to be conducted. Therefore, four levels of damping were investigated: their values, in terms of structural decrement logarithm δ_s, were estimated through free-vibrations tests as 0.034, 0.038, 0.044 and 0.055, corresponding to 0.54%, 0.60%, 0.70% and 0.87% in terms of damping ratio ξ. These estimated damping ratios were seen not to be affected by the magnitude of the vibration for the investigated range of interest. For each test (characterized by a mean value of the wind tunnel velocity), the acquisition was 2 min long, while the sampling frequency was set at 200 Hz.

This first batch of results made possible the association of different peaks of the dynamic response with a local resonance occurring in different regions of the structure. To corroborate these hypotheses, additional investigations were carried out concerning the variation of the shedding frequency along the height of the model. This was possible through the installation of an hot-wire anemometer (HWA) downstream the model. The device used in this type of measurements was a dual-sensor probe with cylindrical sensors provided by Dantec Dynamics. In particular, the configuration 55P61 was
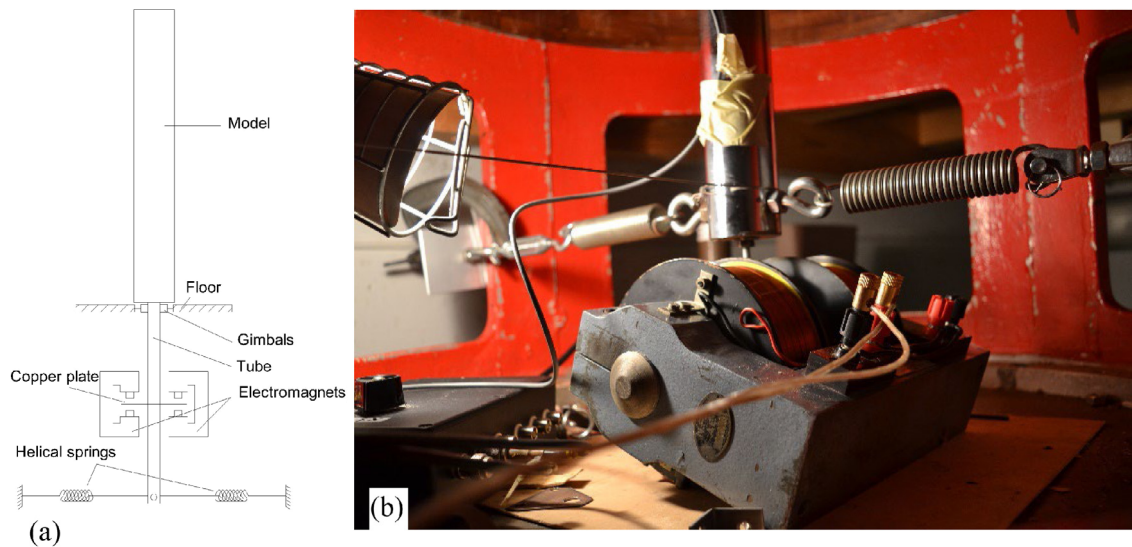
Fig. 4. Single mode-model: (a) scheme of the structure (following the drawing by Walshe, 1972); (b) dynamic rig of the model under the wind tunnel floor.
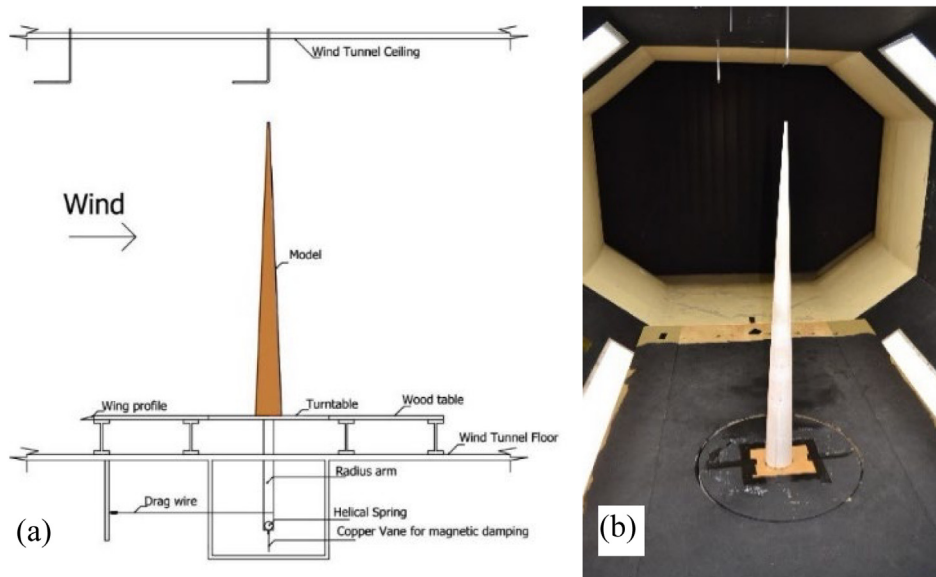
Fig. 5. Layout of the dynamic rig: (a) side view; (b) wind tunnel view.

the adopted one. This probe was installed at four different heights (Fig. 6a), and the tips of these sensors placed 50 cm ($\sim 7D_{ref}$) downstream the model. To investigate the aeroelastic case, the model was let free to oscillate under the effect of the lowest level of structural damping ($\xi = 0.54\%$) amongst those listed before. Accordingly, the wind speed range of the tests was the same as in the accelerometer case. The sampling frequency was set at 200 Hz, and each sample was 2 min long. Fig. 6b shows a picture of the wind tunnel with the HWA installed at a height of 480 mm (position P2).

2.2.2. Pressure model

As it will be clarified in Section 3.1, the highest peak of the structural response occurs when the harmonic content determined through the HWA in position P2 is in close agreement with n_0. Consequently, the region identified by P2 seems to be connected with the maximum dynamic response. To further study this aspect, four different rings of pressure sensors were installed around this portion of the wind tunnel model (Fig. 7b), named as Ring 1–4. Ring 1 and Ring 2 were installed below the area individuated by P2, whereas Ring 3 and 4 above it. Each ring was composed of 16 different pressure taps, equally radially spaced along the relevant circumferences (Figs. 7a and 7c). It was not possible to have additional
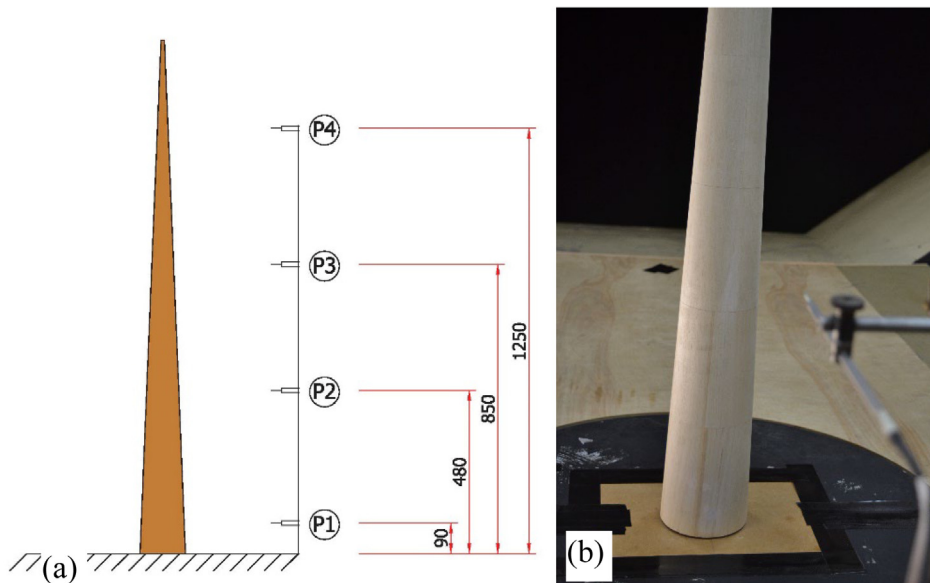
Fig. 6. HWA measurements: (a) heights that have been investigated; (b) close-up for the HWA installed at position P2.
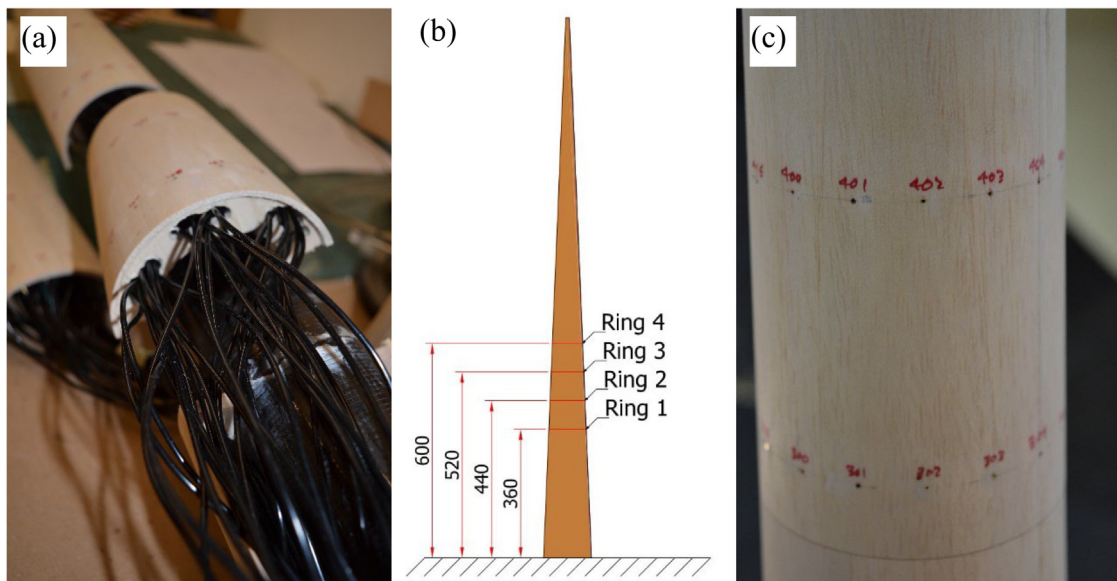

Fig. 7. Pressure measurements: (a) installation of pressure taps; (b) disposition of rings of taps; (c) close-up of the wind tunnel model.

regions equipped with pressure taps due to space constraints within the cylinder, as well as because of the challenges associated with instrumenting the tip of the structure. The 64 pressure channels were measured using a simultaneous multi-channel low range pressure scanning system. The raw pressure measurements were treated with the frequency correction technique for both amplitude and phase distortions (e.g., Kay et al., 2020), taking the length of the tubes into account. The sampling frequency was set at 800 Hz. A high-frequency pressure integration analysis conducted in the frequency domain allowed the local aerodynamic properties of this region of the model to be analysed in detail, in particular the local steady-state drag coefficient and the local unsteady lift coefficient.

The presence of the 64 tubes inside the wind tunnel model introduced additional damping to the system, making it challenging to directly compare its aeroelastic response with measurements obtained through the accelerometer and the hot-wire anemometer. Therefore, the wind tunnel pressure measurements were conducted on a static model, which is the standard set-up for aerodynamic measurements, besides it avoids the potential squeezing of the tubes induced by the structural oscillations.
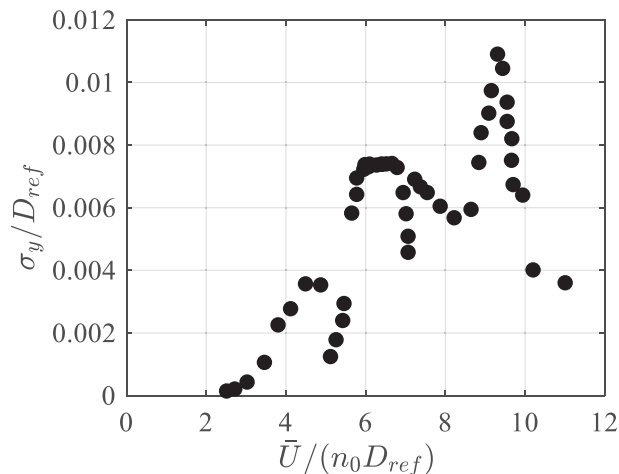
Fig. 8. VIV response of the tapered circular cylinder for the lowest level of damping ($\xi = 0.54\%$).

## 3. Dynamic tests

3.1. Dynamic response

This section of the paper presents the results obtained from the aeroelastic model. This is assessed by evaluating from each time–history of the crosswind displacement y the relevant standard deviation σ_y. The classical VIV response curve of three-dimensional parallel-sided structures may be characterized by a double peak (e.g., ESDU 96030, 1998), induced by the resonant excitation with the main span region (for a lower wind velocity) and the tip region (for a higher velocity). The lower is the level of defence of the structure with regard vortex-shedding (i.e., low Scruton number), the larger the curve might become, due to the occurrence of the lock-in phenomenon. In contrast to that, the non-dimensional VIV response σ_y/D_{ref} pictured in Fig. 8 (for the lowest level of structural damping, $\xi = 0.54\%$), shows three distinct regions, characterized by three different local peaks which are separated by zones where the response drops.

Of particular interest are the responses shown in Fig. 8 around $\overline{U}/(n_0 D_{ref}) \approx 4.6$, 6.5 and 9.4. These three will be referred to as Region 1, 2 and 3 in the following. The maximum response is evaluated as $\sigma_y/D_{ref}\big|_{max} = 0.011$, found in correspondence of Region 3. The presence of different peaks points out a large range of the dynamic response amplification associated with vortex-shedding. As a matter of fact, this seems to be wider than those typically linked with parallel-sided cylinders, as noted by other researchers (e.g., Balasubramanian et al., 2001).

The next set of results here presented are focused on the time-varying nature of the response of the aeroelastic model. From the relevant literature, it is well-known that in the lock-in region the response features a sinusoidal trend, since in this condition the vortex-shedding is governed by the movement of the structure itself on one of its modal shapes (i.e., condition of fluid–structure interaction). Conversely, when the Scruton number is sufficiently high, the action induced by vortex-shedding is simply an aerodynamic one, presenting therefore characteristics that are associated with "forced-random-vibrations". This remark is exemplary explained by Vickery and Basu (1983). Inspecting the evolution of the time-histories reported in Fig. 9a, it is possible to qualitatively observe different regimes occurring in the VIV response, which continuously alternate with the variation of the wind velocity. Specifically, the first two peak regions are apparently characterized by a marked fluid–structure interaction. The third and highest peak instead appears to be more random in nature. Moreover, the three regions are interspaced by intermediate branches featuring a sudden drop in the response, characterized this time by a more random character. In addition to the temporal description provided by Fig. 9a, b–d illustrate the spectral characteristics of the three VIV regions, whose positions on the VIV response curve are indicated in the small graphs included within each sub-plot. The spectra are evaluated through the Welch's technique. The dominant frequency consistently corresponds to the natural frequency of the system (i.e., 9.1 Hz, Section 2.2.1, drawn with a dash-dotted line). However, variations can be observed as the flow velocity changes. Specifically, if the spectra associated with Region 1 (Fig. 9b) predominantly exhibits a single resonant peak, the spectral properties in Region 2 (Fig. 9c) reveal the presence of an additional peak, sitting on 6.5 Hz. This peak coalesces with the structural one in Region 3 (Fig. 9d), leading to a broader peak (at 9.1 Hz) compared with the other two regions, reflecting the more random character observed in the corresponding time-histories. Finally, an increase in the harmonic contribution at higher frequencies (i.e., greater than n_0) is noted with the increase of the wind velocity.

The pattern pictured in Fig. 9a is fairly unusual when compared to the classical finding for parallel-sided cylinders, especially because the predominantly deterministic peaks are not associated with the highest structural response. To further enhance the presentation of these varying trends, the peak factor g_y of the different measured time-histories
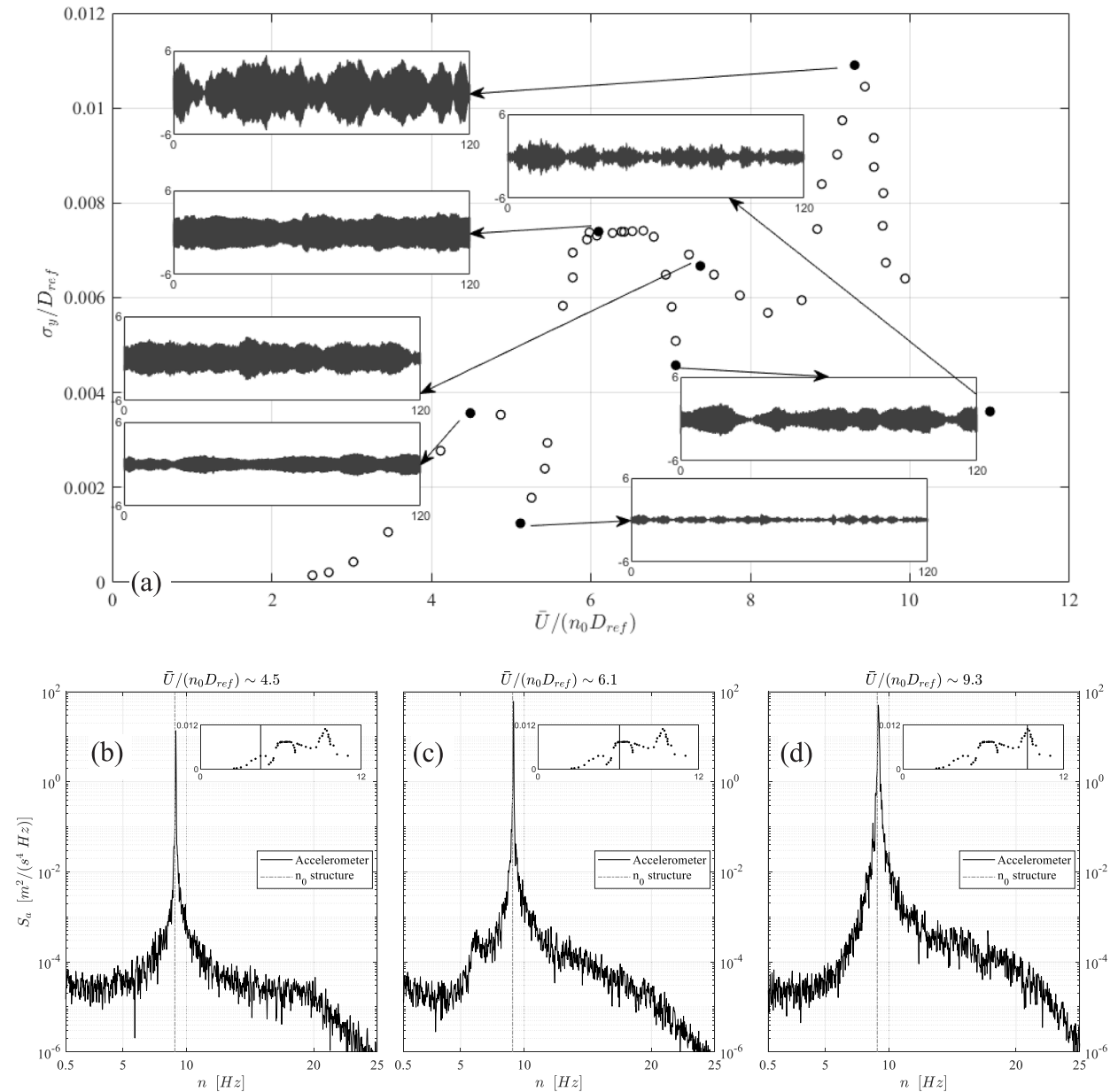
Fig. 9. VIV response and evolution of the time-histories (a), and frequency content (b, c, d) for the lowest level of damping in smooth flow ($\xi = 0.54$ %).

has been evaluated and presented in Fig. 10. It should be noted that values close to $\sqrt{2}$ are associated with a response featuring sinusoidal characteristics (i.e., it is dominated by a single harmonic), while higher values highlight the presence of a more random vibration (3.87 corresponds to broad-banded Gaussian processes).

By combining the outcomes of Figs. 10 and 9a, it is possible to associate with Region 1 peak factors close to 2.0 – 2.15. Even lower peak factors (about 1.9) are linked with Region 2, for a considerable extension. On the other hand, the intermediate branches which anticipate and follow them and featuring a remarkable drop of the dynamic response, are characterized by higher peak factors. Furthermore, in Region 3 (where the maximum displacements occur), a higher peak factor is observed compared to Regions 1 and 2 (albeit still lower than 3). This finding corroborates the visual observations from the time-histories in Fig. 9a and aligns with the spectral analysis presented in Fig. 9b–d.

It is now considered the effects of an increase of the structural damping on the VIV response. In doing so, Fig. 11a–b–c show the relevant response curves for damping ratio $\xi = 0.60\%$, 0.70% and 0.87%, respectively.
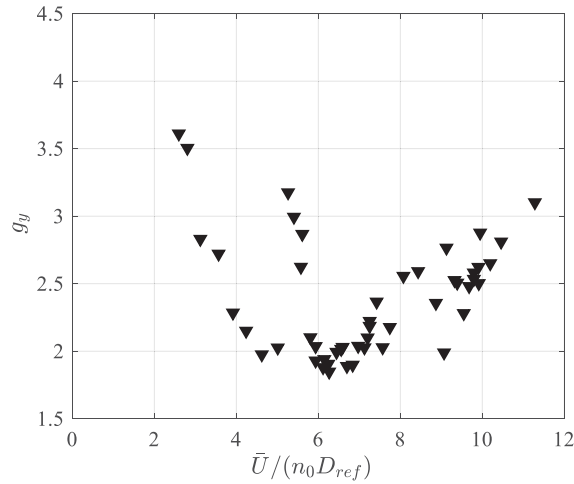
Fig. 10. Peak factors referred to the VIV response reported in Figs. 8 and 9.
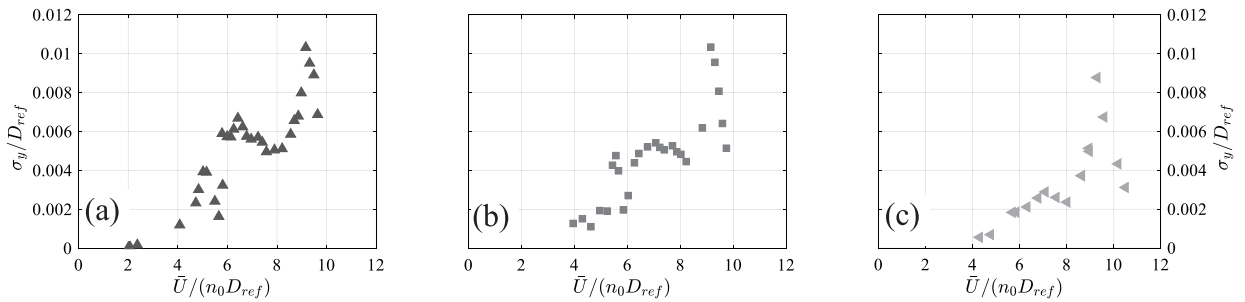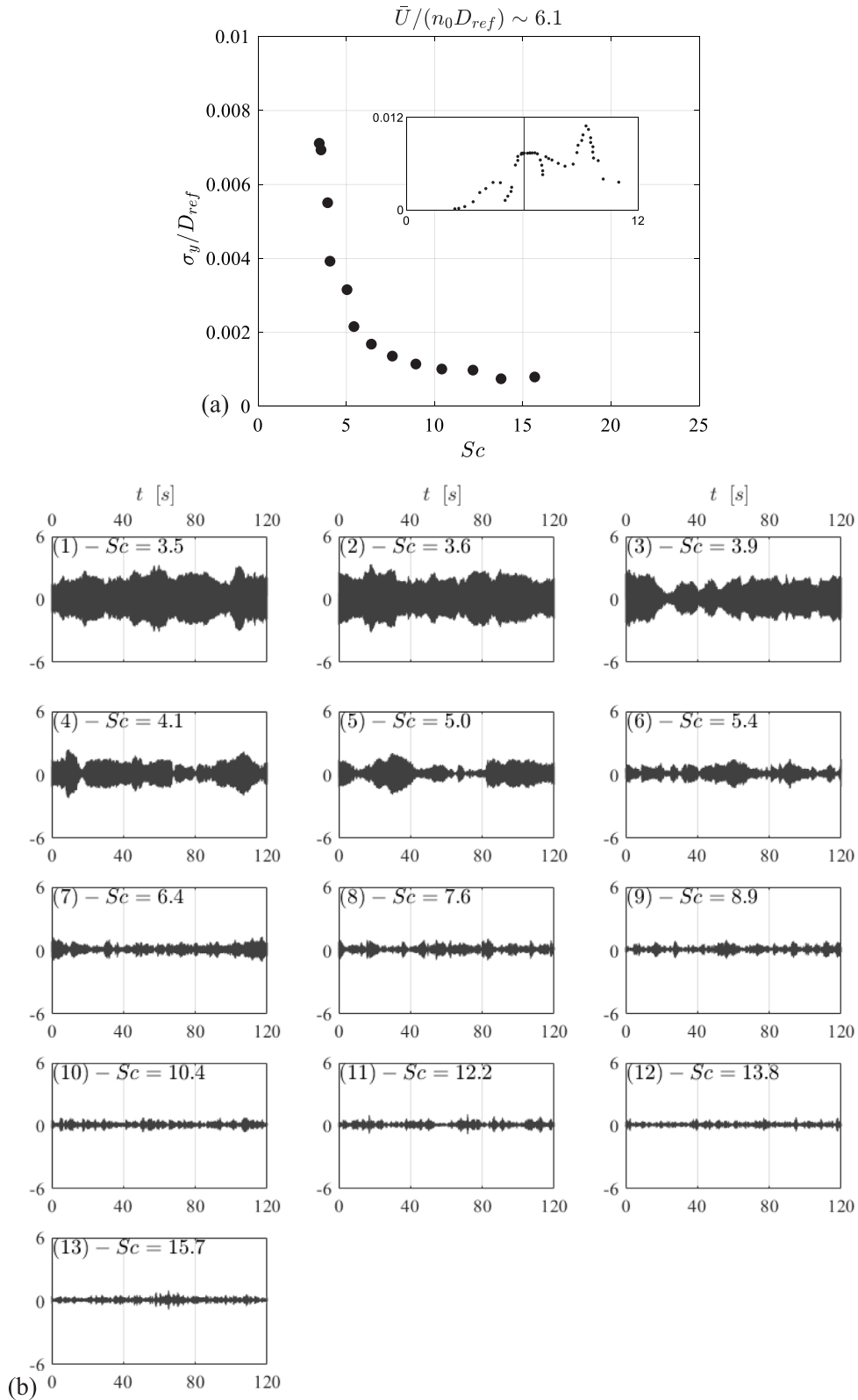

Fig. 11. VIV responses for different levels of damping ratio: (a) $\xi = 0.60$ %, (b) $\xi = 0.70$ % and (c) $\xi = 0.87$ %.

These sub-plots further clarify the difference between the VIV response in the three different regions. An increase of ξ in the first two regions translates in a remarkable reduction of the oscillations. For instance, a growth of the structural damping of the order of 60% (ξ varied from 0.54% to 0.87%) is reflected into a similar reduction in the amplitude of the response in Region 2 ($[\sigma_y/D_{ref}]_{max}$ drops from 0.0074 to 0.0029). The response near Region 1 seems to be heavily influenced by damping, being excited for slightly higher velocities (Figs. 11a and 11b), before eventually being fully mitigated and disappearing (Fig. 11c). On the other hand, the response linked to Region 3 undergoes a more limited reduction, of the order of 20% (diminishing from 0.0109 to 0.0088). These findings are yet another indication that points out the different nature of the VIV affecting the three regions. In fact, it is well-known that deterministic vibrations generally are much more sensitive to the damping ratio (e.g., Kwok and Melbourne, 1981), while the mitigation of random ones is less influenced by this quantity.

Finally, additional tests have been carried out in correspondence of Region 2. In particular, a total of 13 different levels of damping ratios have been explored for the same wind velocity. The results are enclosed in Fig. 12a–b. Taking inspiration from the documents by Vickery (1981) and Vickery and Basu (1983), based on the experimental data obtained by Wooton (1969) on aeroelastic tests of uniform circular cylinders, Fig. 12a shows the VIV response against the Scruton number $Sc = 4\pi m_{eq}\xi/(\rho D_{ref}^2)$. The wind velocity set for these additional tests is also indicated (vertical line in the small graph included within Fig. 12a). To complement this graph, Fig. 12b depicts the corresponding evolution of the 13 time-histories of the acquired acceleration. The order to be followed moves from the left to the right and from top to bottom, as clarified by the numbers (1) – (13) on the top left-hand corner of the sub-plots. Furthermore, these are also enriched with the numeric quantification of the corresponding Scruton number.

As discernible from Fig. 12a, the results are qualitatively similar to those reported by Vickery and Basu (1983), Fig. 9 of their paper, however in a log–log plot which tends to compress the points with higher amplitude). The VIV "transition" regime roughly coincides with the range $Sc = 4 - 6$, while for higher values of Sc the time-histories are dominated by random behaviour (see (7)–(13), in Fig. 12b). The first two points with lower Scruton number ($Sc = 3.5 - 3.6$) show a tendency towards the "lock-in" regime, since their time-histories unveil a quite developed VIV, as reflected by their peak factors, these being close to 1.9–2.0 (Fig. 10). Nevertheless, the maximum response is significantly lower, approximately of an order of magnitude, than the results presented by Wooton (1969). Indeed, Wooton's data were characterized by

Fig. 12. Effect of different levels of damping on the VIV response of Region 2: (a) Dimensionless across-wind response; (b) (1)–(13) evolution of the acceleration time-histories with increasing structural damping (from the left to right and from the top to bottom).

Table 1

Comparison between data relevant to the maximum VIV response from different studies.

Reference	Wooton (1969)	Lupi et al. (2021)	Scruton (1963)	Present paper
$\dfrac{H}{D}$	11.5	15.5	~ 32	21.4
Diameter taper (%)	0	0	~ 4.3	8
ξ (-)	0.0022	0.003	0.0022	0.0054
Sc (-)	3.93	2.94	–	3.5
I_u (%)	Smooth flow	4.4	Smooth flow	Smooth flow
Re	6×10^5	2.3×10^4	Subcritical regime	1.6×10^4 2.0×10^4 2.9×10^4
$\sigma_y/D_{ref}\big|_{max}$	0.15	0.22	–	0.0035 0.0074 0.011
$A/D_{ref}\big|_{max}$	–	0.34	~ 0.06 ~ 0.08 ~ 0.13	0.0071 0.014 0.025

values of $\sigma_y/D_{ref}\big|_{max}$ up to 0.150, while the oscillations presented in this study barely reach a $\sigma_y/D_{ref}\big|_{max}$ of 0.011 (Region 3). In addition, this quantity seems to be lower also when compared with other two selected studies, herein deepened. The first study, which focuses on a cantilevered structure characterized by a constant circular cross section, has been recently published by Lupi et al. (2021). The second one is an investigation documented by Scruton (1963) on a full aeroelastic model of a tapered stack with a lower taper ratio than the one adopted in the present study. Focusing on these three references (plus the case under investigation), Table 1 lists the key parameters driving the VIV phenomenon. Clearly the geometry of the wind tunnel model is an important parameter, in particular a higher slenderness translates into a considerable increase of the structural peak amplitudes, as clearly identified by Wooton (1969). Structural damping ξ and Re are also key parameters to identify the difference between the various experiments. Actually, the effects associated with Re in all VIV experiments are known to be dominant (Sarpkaya, 2004). It is noted that the structural response presented in the paper by Scruton (1963) has been estimated from the graphs there reported and, in particular, the oscillation amplitude has been considered as the amplitude of the response $A|_{max}$. As concerns the paper by Lupi et al. (2021), the values in Table 1 are associated with the case having the lowest level of structural damping.

The maximum response observed in this investigation is significantly lower than the other cases, leading to a discussion on the factors that may contribute to this discrepancy. The analysis primarily focuses on two key aspects that could account for variations among the different studies: taper ratio and slenderness. Firstly, a comparison is made with the results of the tapered structure tested by Scruton (1963), whose response curve is characterized by three different structural peaks. Commenting the results, Scruton stated that *"... a first speed range for instability occurred in the fundamental bending mode, and was followed with increase of wind speed by two distinct speed ranges for instability in the first harmonic mode ..."*. Analysing the critical velocities and the dimensions of the structure, he could associate the first two peaks with the excitation of a diameter near the top of the stack, while he attributed the last peak to the excitation of a diameter close to the bottom of the stack. Therefore, his explanation seems coherent with what discussed before for the case of interest, which is regarded as simpler being a single-mode model. Comparing the 3 peaks from Scruton's studies ($A/D_{ref}\big|_{max} = 0.06, 0.08, 0.13$, Table 1) with those measured in the present study ($A/D_{ref}\big|_{max} = 0.0071, 0.014, 0.025$, Table 1), the magnitude of the firsts leads to a higher response than what reported for the case under investigation. It should be noted that the turbulence intensity is comparable, while the precise Reynolds number range tested by Scruton has not been declared, but it is likely to be within the subcritical regime. On the other hand, the full aeroelastic model tested by Scruton is characterized by a higher level of slenderness and a lower level of tapering, therefore its correlation length for the crosswind forces along the axis should be higher. In addition, the level of structural damping is less than half of what estimated from the experiment discussed in this paper, likely leading to a lower Scruton number. All these factors might explain why the results reported by Scruton are higher of, at least, a factor 3.5.

Comparing the results of the present study with those of the two parallel-sided structures study, the differences become more pronounced, in particular when considering the values by Lupi et al. (2021), which, despite similar values of Scruton number and a higher value of turbulence, are consistently higher than the ones by Wooton (1969). This is clearly shown in Fig. 13, which is equivalent in terms of presentation to Fig. 12a. These differences between the three studies could be a result of the different Reynolds number range tested, as well as the slenderness ratio, but the taper effect is likely to play the major role.

Recalling the considerations made in Introduction concerning the patterns of shed vortices along the height of a tapered cylinder, one can attempt to establish a connection between the first two peaks, which exhibit a relatively deterministic nature, and a variation of the shedding regime (i.e., with a variation of Strouhal number, Vickery and Clark, 1972) occurring at different heights of the model. The first peak should be related to a local synchronization occurring in the upper part
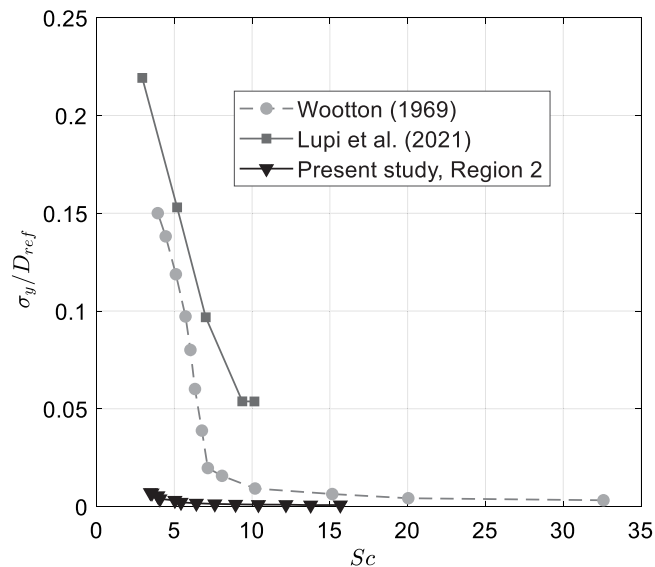
Fig. 13. Variation of the non-dimensional VIV response for different Scruton numbers: comparison between different investigations: Wooton (1969), Lupi et al. (2021), Region 2 (Fig. 12a).

of the model, if compared with the second one. This assumption seems also to be coherent with the observed variation of the spectral properties of the dynamic response (Fig. 9b–d). In particular, the additional peak noted in Fig. 9c at 6.5 Hz may be likely attributed to VIV forces acting in the lower portion of the cylinder. This peak becomes resonant with the natural frequency of the system in the third region (Fig. 9d), hence contributing to a broader spectral response compared with the previous ones, potentially indicating an increased presence of turbulence in the flow (e.g., Vickery and Clark, 1972). As a result, this can lead to a dynamic response characterized by more random characteristics, as those observed in Region 3. The relatively higher harmonic content observed after the predominant peak in the spectra of Regions 2 and 3, compared to the Region 1 (Fig. 9b), are likely to be attributed to vortex-induced actions occurring at frequencies higher than the natural frequency. These actions are primarily localized in the upper portion of the tapered cylinder.

The relatively minor contribution of the fluid–structure interaction in Region 3 (in comparison to Regions 1 and 2) may also be physically explained by considering the different magnitude of the modal amplitude associated with the analysed portion of the model. In fact, when this value is higher (i.e., excitation of Region 1 and Region 2, located in the upper part of the model), the dynamic effects are favoured and so is the interaction between fluid and structure. Conversely, the low modal amplitude associated with Region 3 (located towards the bottom of the model), combined with the broadness of the spectrum, diminishes its impact. As a result, the excitation in this region appears as more random in nature. The use of the hot-wire anemometer, whose results are described in the following Section, will shed lights about these remarks.

3.2. Analysis of the wake

The data gathered by placing an HWA (Section 2.2.1) downstream of the model at four different heights (Fig. 6a) have been elaborated with the aim of estimating the spectral content of the acquired signals through the Welch's technique, in particular focusing on the lateral component (i.e., corresponding to the crosswind response of the model). Salient results are reported in Fig. 14a–b–c, where each sub-plot depicts the four spectra of the lateral component acquired by the HWA for a different reduced wind velocity (indicated in the title of the sub-plot). These three graphs focus on the structural peaks detectable in Fig. 8, which, for clarity, is also shown in small graphs included within each sub-plot, as already done in Fig. 9b–d. Moreover, in each sub-plot a vertical dash-dotted line is drawn, which traces the natural frequency of the model n_0 (9.1 Hz).

From a general point of view, the ensemble of the data allows one to verify that, for a selected wind speed, the shedding frequency moves from top to bottom, becoming lower. Starting with the analysis of the lower velocity (Fig. 14a), the HWA in position P3 (upon hereinafter the term "position" will be avoided, and simply recalled by the corresponding "P" name) captures a harmonic content definitely close to the natural frequency of the structure, suggesting that the first structural peak might be induced by a local resonance occurring in correspondence of P3. The hot-wire anemometer in P4 shows a much higher harmonic content (whose peak sits on ~19.8 Hz). This means that the region associated with P4 (the tip of the model) is not interested by a local resonance. On the other hand, the measurement in P2 and P1 depict a peak at 5.1 Hz. The spectra associated with P3 and P2 are denoted by a quite sharp peak, conversely P1 appears to be affected by a broader nature, perhaps because of the influence of the residual boundary layer and the complex flow in its
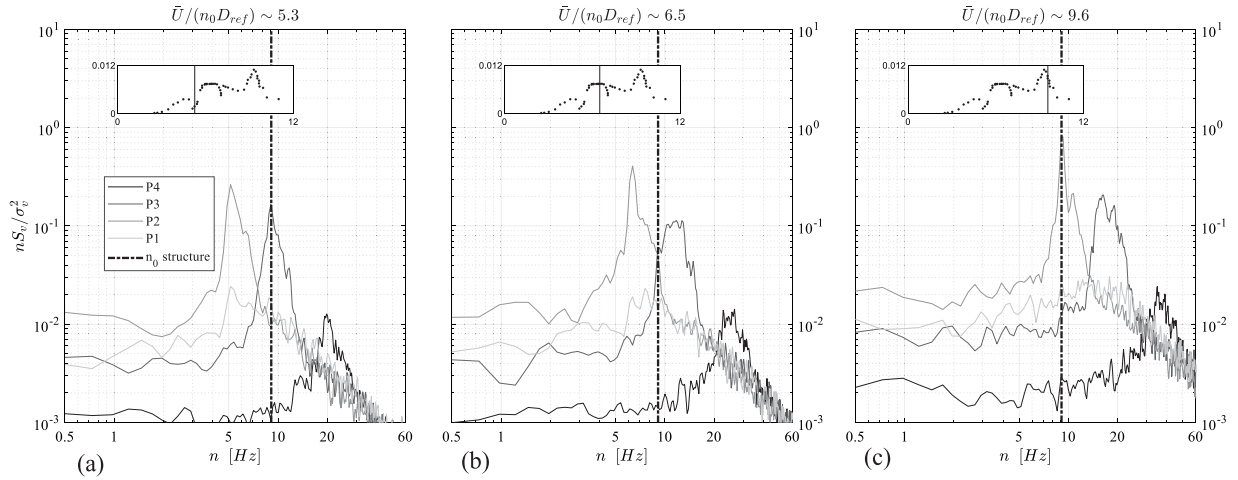
Fig. 14. Spectral content estimated from HWA measurements at different heights and different wind velocities: (1) $\overline{U}/n_0 D_{ref} \sim 5.3$; (2) $\overline{U}/n_0 D_{ref} \sim$ 6.5; (3) $\overline{U}/n_0 D_{ref} \sim 9.6$.

proximity (Peterka et al., 1985). It is also worth noting that, in spite of the resonance occurring in P3, the spectra content measured at P2 is higher, suggesting that the local forced excitation may be stronger that the resonant phenomenon occurring at 850 mm. However, as a note of caution, comparisons in terms of magnitude between the different spectra may be misleading since they derive from non-simultaneous measurements. Moving on to the analysis of Fig. 14b (second structural peak), neither P2 nor P3 captures a harmonic content close to the natural frequency of the structure, which is in the middle of them, inferring that the second structural peak might be linked with a local resonance of the model occurring in a region between P2 and P3. Now the spectra of P4 and P3 are clearly broader than in Fig. 14a, whereas the spectrum relevant to P2 is still quite narrow, and it is again higher in magnitude than all the others. Its peak sits on 6.4 Hz, which is in close agreement with the aerodynamic one detected by analysing the dynamic response for this Region (Fig. 9c). Concluding the analysis with the third peak (Fig. 14c), the measurement in P2 reflects a dominating frequency which is in close agreement with the natural frequency of the structure. Consequently, it seems now possible to state that the highest structural displacement of the model may be ascribed to a local resonance happening close to P2, where the modal amplitude is reduced and consequently the response has more forced than aeroelastic characteristics. This constitutes a remarkable difference with the case of parallel-sided cylinders, whose tip excitation is known to be crucial for VIV (see, e.g., ESDU 96030, 1998). In the case here analysed, the resonance at the tip occurs for low wind speed, whose synchronization with the structure is associated with a modest level of energy, which is exceeded by the (albeit forced) excitation of the bottom of the model, occurring for higher wind velocities.

Since the region of the model associated with P2 was found to be linked with a local resonance (Fig. 14c) leading to the highest structural response, additional studies have been conducted in its proximity, this time to investigate the aerodynamic properties of the model, which will be documented in the next Section.

4. Static tests

The presence of 16 pressure sensors for each ring of taps (Fig. 7a–c) installed in the portion of the model close to P2 and sampled simultaneously at 800 Hz, assured a great resolution in frequency to study the spectral content of the crosswind response at different heights. In addition, the measured pressure time-histories data were also analysed to quantify the aerodynamic coefficients, both in the alongwind and in the crosswind directions, i.e., the drag coefficient Eq. (1a) and the lift coefficient Eq. (1b) at different heights:

$$c_D(t, z) = \frac{f_D(t, z)}{\frac{1}{2}\rho \overline{U}^2 D(z)}, \tag{1a}$$

$$c_L(t, z) = \frac{f_L(t, z)}{\frac{1}{2}\rho \overline{U}^2 D(z)}, \tag{1b}$$

where f_D and f_L are the time-histories of the drag and lift forces, $\overline{U}$ is the mean value of the reference wind velocity and $D(z)$ is the local diameter linked with the corresponding coordinate z (Fig. 7b).

Attention is also given to the harmonic properties of the different time-histories of c_L, focusing on the variation of the spectral peaks with the height. The relevant spectra are newly evaluated by adopting the Welch's technique.
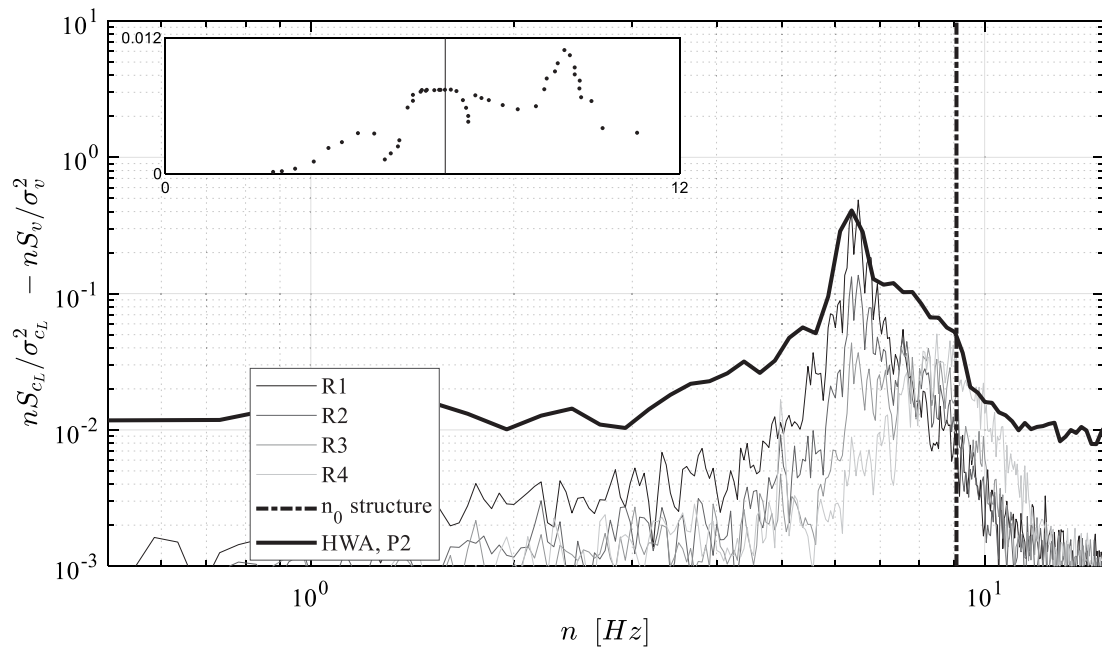
Fig. 15. Spectral content estimated from the four rings of pressure taps and from the HWA in P2 for a $\overline{U}/(n_0 D_{ref}) \sim 6.5$.

Firstly, the consistency between the pressure sensors and HWA measurements, which have been conducted at similar wind velocities, has been checked. An example is shown in Fig. 15, by reporting in the same plot the four spectra of the lift coefficient, S_{c_L}, estimated by integrating the measurements on the four rings (R1-R4), and the harmonic content registered by the HWA at P2 (just placed between R2 and R3) for $\overline{U}/(n_0 D_{ref}) \sim 6.5$ (i.e., Region 2 in Fig. 8). In both cases, the spectra are appropriately made non-dimensional. The thicker black line represents the non-dimensional spectrum evaluated from the HWA, while the thinner lines refer to the four rings R1-R4 that encompass P2 in their elevations. As in Figs. 9b–c–d and 14a–b–c, the natural frequency of the model is indicated through a dash-dotted grey line. This seems to be in proximity of the spectral peak associated with R4, confirming that the resonance leading to the structural peak associated with Region 2 occurs between P2 and P3, hence validating the results from the wake measurements (Section 3.2).

From a general point of view, the comparison between the two techniques seems relatively consistent. However, it is possible to note that the spectra from the pressure measurements are much narrower than that of the HWA, especially for the lowest ring R1. Conversely, the spectrum estimated with the HWA appears quite broad, particularly for the frequency range beyond its peak. Indeed, the corresponding descending slope is less steep than the ascending one, and it appears to embrace also the whole energetic contribution displayed by the superior rings (i.e., R3, R4). The different shapes obtained by using the pressure taps or the hot-wire anemometer might reflect the difference between the level of interference of the measurements and the wake downstream. In fact, the acquisition of the rings is subjected to a low level of interference, while the HWA, placed 50 cm downstream, is positioned in the far-wake, since the typical length required for the formation of the vortices is 2.5 D_{ref}.

Once established a link between the HWA and pressure taps measurements, the focus now moves to an in-depth analysis of the latter ones, in particular concerning a wind velocity related to the highest structural response (i.e., Region 3). In doing so, Fig. 16a reports the relevant spectra in the alongwind direction, thus reporting the spectra of the associated time-history of the drag coefficient Eq. (1a). Likewise, Fig. 16b presents the corresponding spectra in the crosswind direction (i.e., spectra of the lift coefficient, Eq. (1b)). Fig. 16c singularly reports the estimated crosswind spectra for each of the rings for the sake of clarity.

The analyses of the spectra related to the alongwind direction do not present any peak. This is strictly associated with the effect of the taper (see, e.g., Chen et al., 2021a,b). Conversely, the analyses of the lift coefficient immediately reveal the presence of spectral peaks, at a frequency slightly higher than n_0. Fig. 16c clarifies the obvious presence of a resonance occurring at R1 and R2, which share the same shedding frequency, 9.27 Hz. This outcome points out the cellular nature of the vortex-shedding. Nevertheless, the spectrum from R2 is less sharp and lower. When moving to the upper part of the instrumented portion of the model, Fig. 16b–c indicate that R3 displays the presence of several peak, suggesting that this structural height does not belong anymore to the previous vortex cell, but rather it lies in a transition zone. Moreover, the shape of the spectrum does not seem to decrease once the value of 10 Hz is approached, possibly linked with a different vortex cell associated with a higher part of the model. This hypothesis is confirmed by observing the spectrum of the last ring (R4), which indicates a modest peak sitting around 12.25 Hz. It is worth noting that these considerations were made
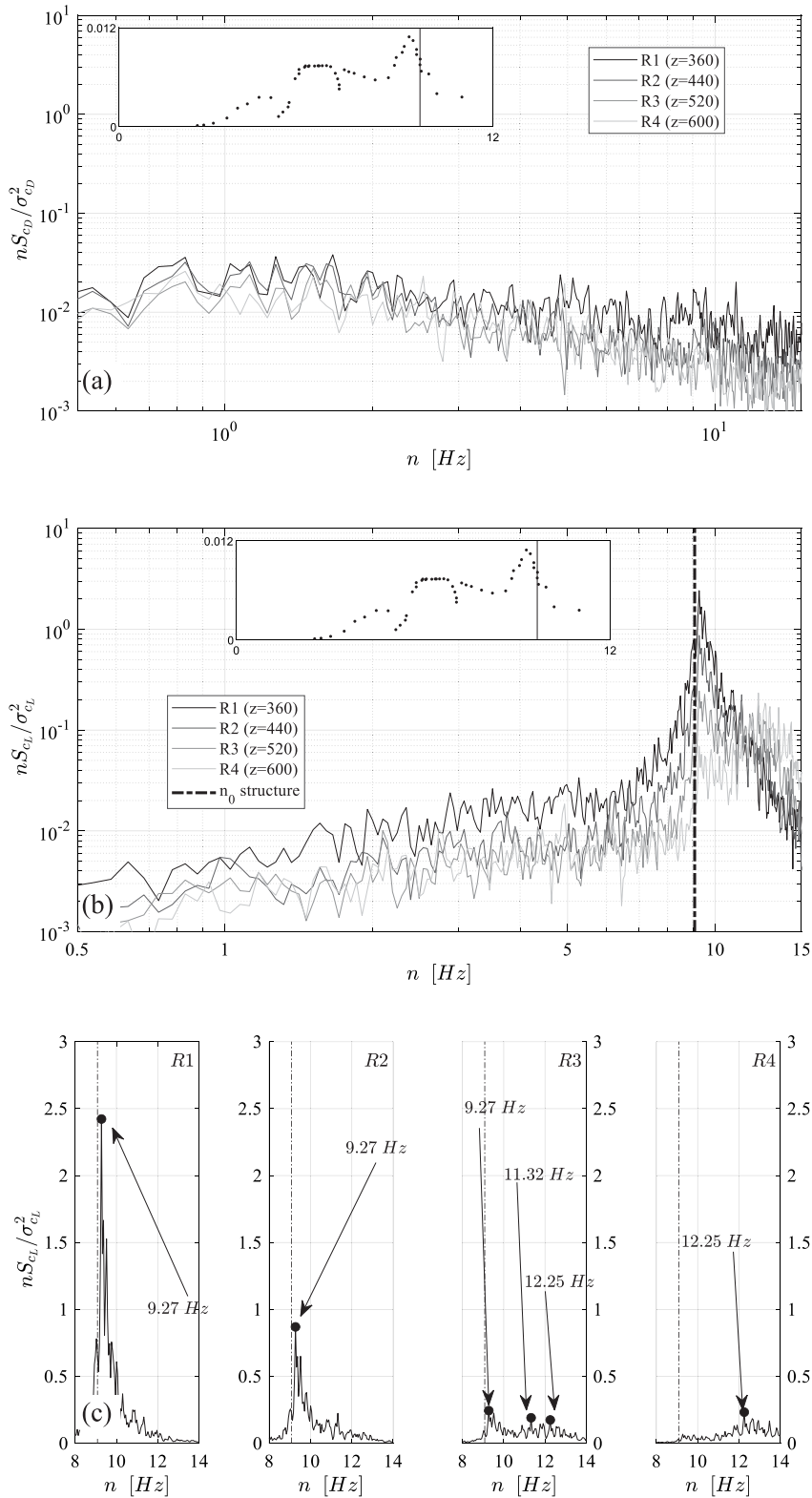
Fig. 16. Spectral content estimated from the four rings of pressure taps, for $\overline{U}/(n_0 D_{ref}) \sim 9.6$: (a) alongwind direction; (b) and (c) crosswind direction.

possible by the simultaneity of pressure taps measurements, which therefore not only confirmed but also enhanced the preliminary findings obtained from HWA acquisitions.

This result can be evidenced by using the continuous wavelet transform (see, e.g., Buresti et al., 2004; Guo and Kareem, 2016), a technique that is well-consolidated for mechanical identification (e.g., Huang and Su, 2007) and that is becoming more and more popular also in structural engineering, e.g., to detect changes in the mode shapes (Solìs et al., 2013). Unlike the discrete transform, the continuous wavelet transform does not have an orthogonal representation, resulting in redundancy. The continuous transform offers, however, a stable representation and allows for the flexibility to select wavelets that possess desirable properties for interpreting the results and applying dynamic filters (e.g., Brusco et al., 2022b). In particular, the complex Morlet wavelet (e.g., Mariotti, 2018) is employed as follows:

$$\psi(t) = e^{i\omega_0 t} e^{-t^2/2}. \tag{2}$$

The Morlet wavelet has an optimal joint time–frequency concentration and provides an excellent compromise between time and frequency resolution. Its output is complex, and if the values of its square modulus are integrated in time, a wavelet spectrum is obtained (e.g., Mariotti and Buresti, 2013; Mariotti et al., 2017), which may be shown to be connected with the Fourier power spectrum averaged by the power spectrum of the wavelet. Particularly for highly non-stationary and modulated signals, the wavelet spectra are smoother than the Fourier spectra and the dominating frequencies may better be highlighted without the necessity of any averaging procedure (which is instead required for the Welch's technique). The wavelet power spectrum can thus be evaluated as:

$$P_{x,W}(a) = \frac{1}{C_\psi} \int_{-\infty}^{+\infty} |W_x(a, \tau)|^2 d\tau. \tag{3}$$

The wavelet transform may also be used to characterize the correlation between two signals, providing not only the time variation of the frequencies simultaneously present in the two signals that contribute to their correlation, but also the phase between the fluctuations at those frequencies. Indeed, if $W_x(a, \tau)$ and $W_y(a, \tau)$ are, respectively, the wavelet transforms of two signals $x(t)$ and $y(t)$, the wavelet cross-scalogram $W_{xy}(a, \tau)$ (Onorato et al., 1997) may be defined as follows:

$$W_{xy}(a, \tau) = W_x^*(a, \tau) W_y(a, \tau). \tag{4}$$

The real part of the cross-scalogram is the co-scalogram CoW_{xy}, which gives the time variation of the contribution of each scale to the correlation between the two signals.

We may then introduce a wavelet local correlation coefficient (Buresti et al., 2004):

$$WLCC(a, \tau) = \frac{ReW_{xy}CoW_{xy}(a, \tau)}{|W_x(a, \tau)| |W_y(a, \tau)|}, \tag{5}$$

which provides the time-local contribution of each frequency present in $x(t)$ and $y(t)$ to their correlation coefficient. Accordingly, its values are comprehended between -1 and $+1$. In particular, the correlation analyses have been carried out in the following between the signals acquired by R1 and the other rings. Synthetically, the results may be expressed by the time-averaged values of the $WLCC$, indicated as $\overline{WLCC}$.

Applying Eq. (3) by selecting $\omega_0 = 6\pi$ (to increase the resolution in frequency, e.g., Brusco et al., 2022a), Fig. 17 reports the wavelet power spectra corresponding to the case of Fig. 16b.

The smoothness characterizing the wavelet technique allows one to identify the presence of a vortex-shedding cell interesting the rings R1 and R2 in an even clearer way. Indeed, the spectral peaks of the three rings towards the bottom (R1, R2, R3) of the model basically coincide, sitting on ~ 9.3 Hz. However, if the spectra linked with R1 and R2 exhibit a single peak, this is no longer true for R3, which is characterized by a second harmonic content, detectable around ~ 12.2 Hz. This second peak appears to be enhanced when moving to the analyses of R4, in which the spectral content seems definitely switched towards a higher range, hence confirming, and indeed clarifying, the findings of Fig. 16c.

Focusing again on the selected value of $\overline{U}/(n_0 D_{ref}) \sim 9.6$ Fig. 18 shows the results concerning $WLCC$, pointing out that the correlation between the lift coefficients linked with R1 and R2 is dominated by a peak close to the natural frequency ($\overline{WLCC}(9.21 \text{ Hz}) = 0.88$). When the correlation moves between the levels R1 and R3, the curve becomes flatter, but it still presents its peak in the same frequency as in the previous case ($\overline{WLCC}(9.21 \text{ Hz}) = 0.53$). Conversely, the contribution to the correlation between R1 and R4 is strongly mitigated ($\overline{WLCC} < 0.25$ at each frequency). These observations encompass a set of information that goes beyond a simple correlation coefficient, whose action inherently filters out the different sources of energy that contribute to the final correlation. If one evaluates this coefficient for the three aforesaid correlations, the values 0.13, 0.04 and 0.03 would be obtained.

Until now, the square modulus of the transform has been used to derive the wavelet power spectrum. Nonetheless, its analysis may be instrumental to develop dynamic filters of the lift coefficient time-histories Eq. (1b), allowing the definition of the part strictly relevant to vortex-shedding and its separation from the one linked with turbulence. This may be done by choosing a threshold value of the energy and applying it to the map: the values above the threshold are identified and maintained for further analyses, while those below it are put to zero. Consequently, the inverse transform is applied, and the extracted signal is equivalent to the application of a particular band-pass filter with continuously
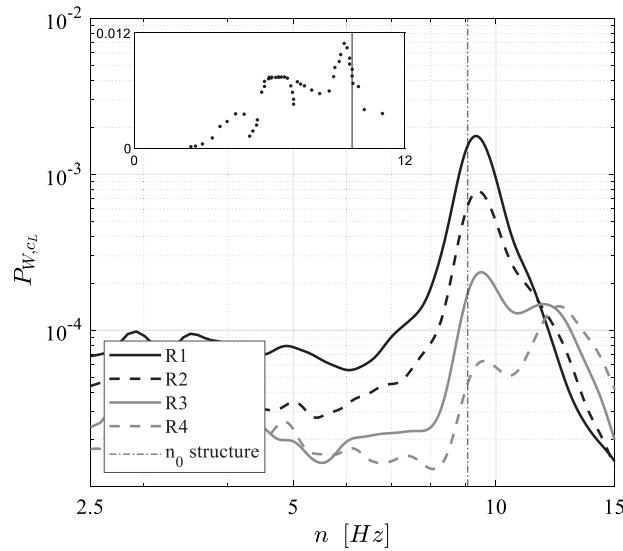
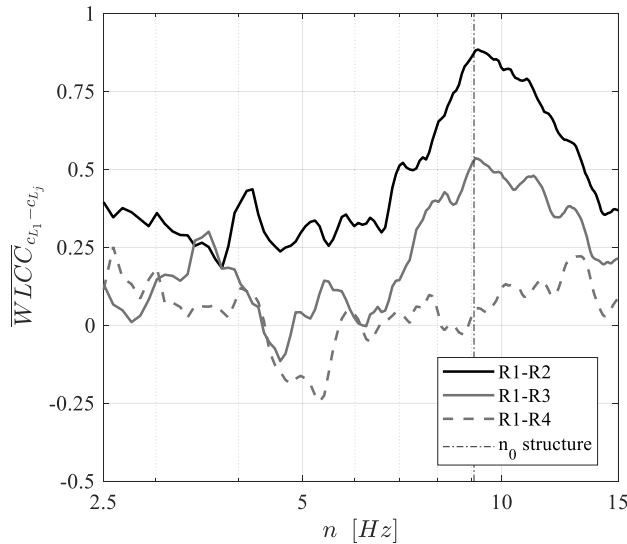Fig. 17. Wavelet power spectra of the lift coefficients of the pressure rings for $\overline{U}/(n_0 D_{ref}) \sim 9.6$.


Fig. 18. $\overline{WLCC}$ for the lift coefficients of the pressure rings for $\overline{U}/(n_0 D_{ref}) \sim 9.6$.

varying multiple bands (e.g., Brusco et al., 2022b,a). For the case of interest, these will be focused on the vortex-shedding frequency.

By analysing the wavelet map of the lift coefficient time-histories of the different rings, it was found that setting a threshold equal to the 45% of the mean energy of the map (studied between 2.5 and 45 Hz, to filter out the presence of turbulence and to isolate the vortex-shedding contribution) was leading to a satisfying result. Nevertheless, analyses for different values of the threshold were carried out as well, verifying the similarity of the outcomes. Fig. 19 shows 2 selected seconds (42–44 s) of the time-histories of the lift coefficients estimated from the four different rings (from top to bottom: R1 to R4), newly for $\overline{U}/(n_0 D_{ref}) \sim 9.6$. The original versions, c_L, are overlapped by the filtered counterparts, $c_{L,W}$ (where the subscript W recalls they have been obtained through wavelet-based procedures).

From this analysis, it is possible to estimate the numerical quantities of the standard deviation of $c_{L,W}$, revealing that these values are strongly reduced if compared with the case of a two-dimensional cylinder. For example, the standard deviation of the coefficient for R1 is 0.06 (Fig. 19a). Once moving to the higher part of the model (i.e., Fig. 19b–c–d), a reduction of the magnitude is observed, likely to be induced by a more pronounced random regime of the vortex-shedding (which is evident from the sequence shown in Fig. 19a–b–c–d).
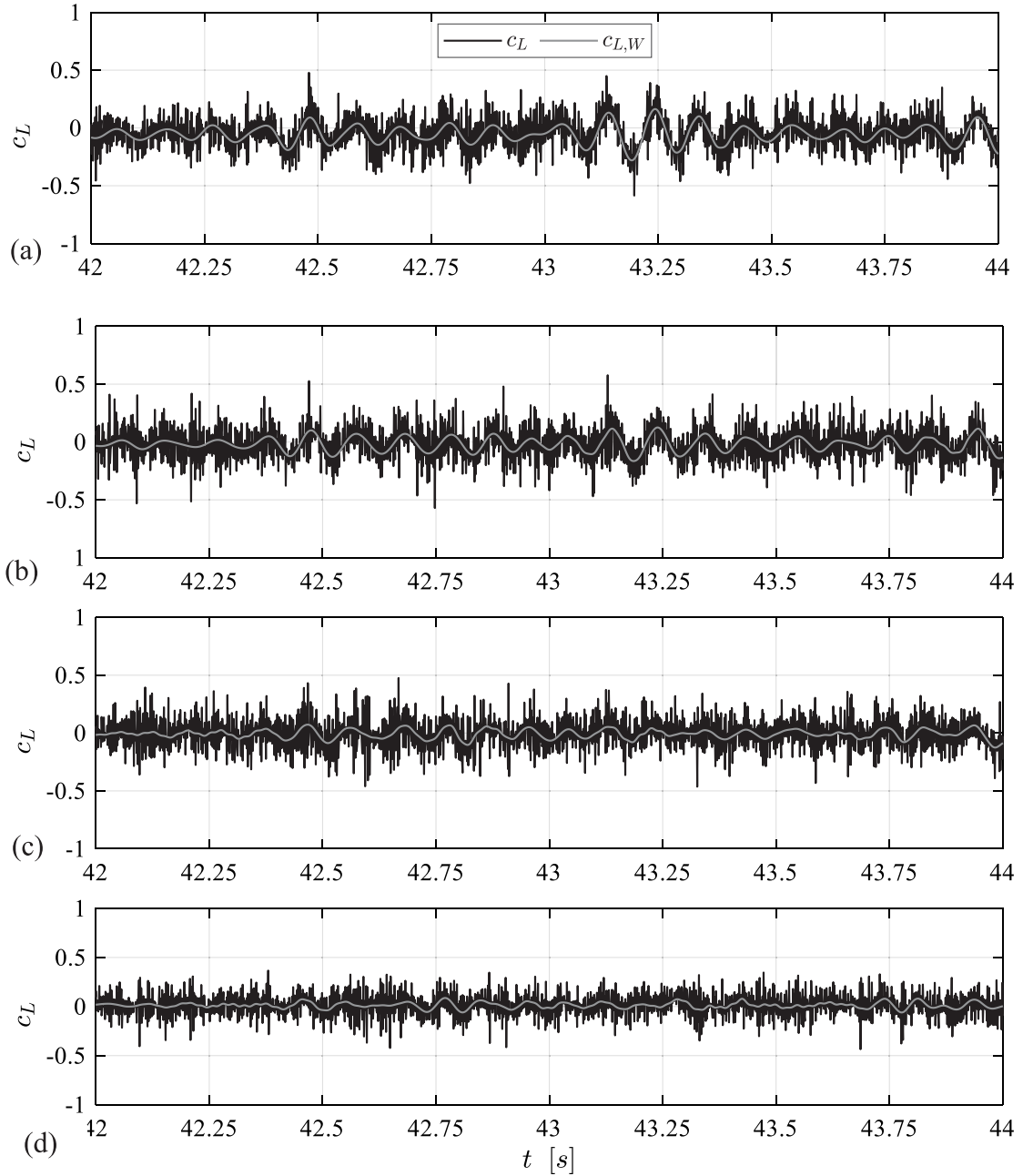
Fig. 19. Original lift coefficient time-histories (black) and filtered version (grey) for $\overline{U}/(n_0 D_{ref}) \sim 9.6$: (a) R1, (b) R2, (c) R3 and (d) R4.

Moving to the analyses of the mean pressure distribution, the evaluation of the j-th mean pressure coefficient may be tackled by the following equation:

$$c_{P,j}(t) = \frac{p_j(t) - \overline{p}_s}{\frac{1}{2}\rho\overline{U}^2}, \tag{6}$$

where p_j is the wind pressure time–history acquired by the j-th pressure tap, and $\overline{p}_s$ is the mean static pressure provided by the upstream Pitot-static tube.

Fig. 20 reports through grey triangles (Wind Tunnel Tests, WTT, R4) the mean pressure coefficient $\overline{c}_P$ distribution estimated in R4 for $\overline{U}/(n_0 D_{ref}) \sim 9.6$. The ordinate ranges from -180 to $+180$ degrees, and its midpoint portrays the location of the stagnation point. The same graph also encloses (black circles) the pressure distribution corresponding to
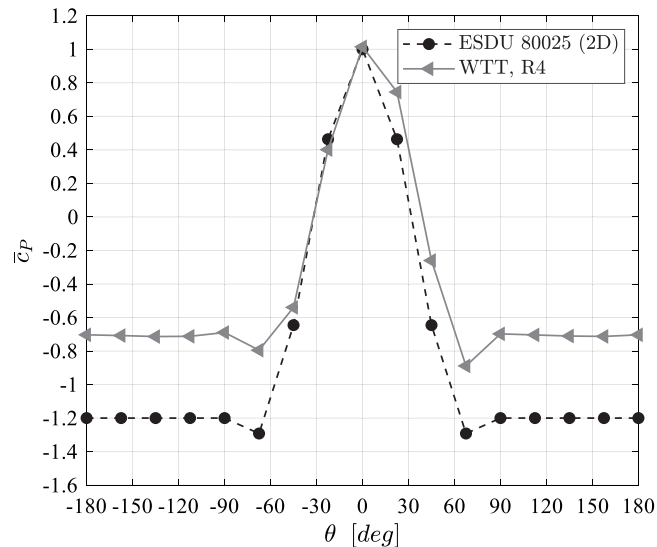
Fig. 20. Comparison between the mean pressure distribution for a 2D circular cylinder (ESDU 80025, 1986) and the one acquired in R4 for $\overline{U}/(n_0 D_{ref}) \sim 9.6$.

parallel-sided circular cylinders, estimated through ESDU 80025 (1986) for the same Reynolds number. By comparing the distributions, it stands out that all the taps in the afterbody are featured by a reduced suction if compared with the two-dimensional case.

This remark anticipates a strong reduction of the drag coefficient (Eq. (1a)) if compared with a two-dimensional case. Indeed, the corresponding estimated mean values from the different rings (in average $\sim$0.90) entail a reduction of 25% if compared with those typical for parallel-sided circular cylinders (i.e., $\sim$1.2, e.g., Blevins, 2001). A similar conclusion is found when comparing the standard deviation of the lift coefficient in the two conditions. Indeed, a typical value for a two-dimensional configuration and the same Reynolds number, is almost 0.5 (see, e.g., ESDU 96030, 1998). Even taking the potential three-dimensional effects related to the finite length of the model into account (e.g., ESDU 96030, 1998 for the lift coefficient, or ESDU 81017a, 1987, for the drag coefficient) seems not to justify this strong reduction.

On the other hand, these coefficients may also be compared with the few contributions in scientific and technical literature concerning tapered circular cylinders. Specifically, the mean drag coefficients seem to be lower than what provided by ESDU 81017a (1987), which predicts a reduction of 10% of the two-dimensional reference for circular structures characterized by a taper ratio equal to 8% of its diameter. This discrepancy may be due the complexity of the wind field at the bottom of the model due to the downward flow directions below the stagnation streamline near the structure along with resulting horseshoe vortices (e.g., Baker, 1979; Wang and Kopp, 2021). On the other hand, it seems coherent with the outcomes highlighted by Vickery and Clark (1972). As concerns the lift coefficient, the values reported about Fig. 19 resemble those found by Vickery and Clark (1972), although somehow smaller, likely because of the higher level of the taper herein documented. Another quantity to be checked regards the position of the vortex cell in resonance with the structure, leading to the maximum response. According to the predictive equation proposed by Vickery and Clark (1972), this position should be located at the height for which the derivative with respect the vertical axis z of the diameter raised to the fourth power, multiplied by the crosswind displacement (herein identified by the modal shape ψ_y), is null. Applying this technique, this height results at 375 mm in the case under investigation, which almost coincides with the position ring R1, whose local excitation was indeed found to lead to the maximum structural response.

5. Conclusions and future perspectives

In the present paper, the outcomes of a wind tunnel test campaign carried out on a highly tapered circular cylinders in smooth conditions are reported. In particular, the experimental campaign seeks to link the studied case with milestones from wind engineering concerning VIVs for tapered circular-shaped systems (Scruton, 1956, 1963; Vickery and Clark, 1972, although all characterized by a lower taper ratio), as well as to point out the cellular nature of the vortex-shedding that occurs in their wake.

Dynamic and static tests have been performed on the structure, by using of different and appropriate instrumentation according to the object of the investigation, which firstly focused on the global behaviour and subsequently moved to local analyses.

The high value of taper reduces the regularity of the detachment of the vortices, which is known to directly affect the values of the non-dimensional aerodynamic coefficients, which may become lower if vortex-shedding is not well-developed (Buresti, 1998). The lift force correlation and displacements in the crosswind direction indeed result strongly reduced when compared with results for parallel-sided cylinders tested at similar Reynolds number (e.g., Lupi et al., 2021). The same observation applies to the values of the mean drag coefficients as well. Nonetheless, the peculiar shape of the response curve (exhibiting three different regions) highlights that the wind velocity range associated with VIV is broader compared with the case of a parallel-sided cylinder. The whole of these results may be attributed to the presence of a cellular vortex-type field, which significantly influences the global dynamic response of the structure. The local excitation of the different cells leads to different response regimes, as reflected by the relevant time-histories and peak factors. The local resonance of a cell closer to the top of the model (associated with an amplification of the response occurring at lower wind velocities) is linked with regimes that look to be quite deterministic, whereas a vibration regime with more random characteristics is noted when the excited cell moves towards the bottom of the structure (higher wind velocities). Accordingly, this is also testified by the role of the damping ratio, whose increase appears to be strongly efficient for the mitigation of the first two structural peaks, while its effect is not that pronounced for the reduction of the third one. The taper is instrumental in framing the vortex-induced response in the local excitation of selected portions of the model. When the wind velocity is low, the excited region is close to the top of the model, being characterized by a large value of the modal amplitude, thus favouring potential aeroelastic effects. However, these are strongly mitigated because of the smallness of the cells and the reduced amount of energy associated with the low wind speed. On the other hand, when the wind velocity is increased, the excited region moves to the bottom of the structure and therefore the vortex cell is likely to become larger, being the local diameter larger. Despite the associated limited value of the modal amplitude and the more random nature of the response, the relevant displacements are higher than those induced by the (aeroelastic) excitation of the upper part of the model due to the higher flow velocity. The preliminary position of this last cell has been detected through the hot-wire anemometer, and this location has been encompassed with the installation of four rings of pressure taps. The linked measurements clarified that its resonance with the structural natural frequency was associable with the maximum response, confirming the preliminary hot-wire anemometer outcomes. This position seems to be predicted also by using the indications provided by Vickery and Clark (1972), therefore verifying their formulation. This outcome is promising as it allows for a preliminary assessment of the height of the critical cell and its associated dynamic response, to be verified in further investigations. Furthermore, the corresponding reduced values of the mean drag coefficient and standard deviation of the lift coefficient highlight a significant mitigation of the vortex-shedding phenomenon when compared to the two-dimensional configuration. This effect is likely attributed to the high taper ratio of the investigated element.

Wind codes and guidelines hardly provide support for engineers for the design of tapered structures, whose behaviour to wind actions does strongly differ from a parallel-sided cases. The data herein gathered might serve as a stimulating input for analysing tapered structures characterized by different taper ratios and slenderness, especially with the aim of improving the knowledge of parameters relevant to vortex-shedding (e.g., limiting amplitude, standard deviation of lift coefficient, drag coefficient). Additionally, these findings could have potential applications in the calibration of reduced-order models, as explored in previous studies (e.g., Basu and Vickery, 1983; Vickery and Basu, 1983; ESDU 96030, 1998; Pagnini et al., 2020; Guo et al., 2021), the improvement of which appears crucial for the optimization of structural behaviour to wind loads (e.g., Zuo and Letchford, 2010). Future experimental campaigns should focus on in-depth studies of the cellular nature of the vortex-shedding generated by such structures, by employing advanced flow visualization techniques such as PIV.

Dedication

The authors wish to dedicate this work to the memory of Professor Tom Wyatt, who was the designer of the wind tunnel model object of this paper, as well as the main promoter of this research. His passion, care and technical knowledge were instrumental in setting up the wind tunnel test campaign carried out. Afterwards, as he had been doing throughout his career, he faced with unique enthusiasm the challenges offered by the interpretation of the results, providing continuous feedback and essential guidance.

CRediT authorship contribution statement

Stefano Brusco: Data curation, Formal analysis, Investigation, Methodology, Software, Visualization, Writing – original draft. **Anna Bagnara:** Conceptualization, Funding acquisition, Investigation, Methodology, Project administration, Resources, Supervision, Validation, Writing – review & editing. **Stefano Cammelli:** Conceptualization, Funding acquisition, Investigation, Methodology, Project administration, Resources, Supervision, Validation, Writing – review & editing. **Giuseppe Piccardo:** Conceptualization, Funding acquisition, Investigation, Methodology, Project administration, Resources, Supervision, Validation, Writing – review & editing.

Declaration of competing interest

The authors declare that they have no conflict of interest.

Data availability

Data will be made available on request.

References

Baker, C.J., 1979. The laminar horseshoe vortex. J. Fluid Mech. 95 (2), 347–367. http://dx.doi.org/10.1017/S0022112079001506.

Balasubramanian, S., Haan, F.L., Szewczyk, A.A., Skop, R.A., 1998. On the existence of a critical shear parameter for cellular vortex shedding from cylinders in non-uniform flow. J. Fluid Struct. 12, 3:15. http://dx.doi.org/10.1006/JFLS.1997.0122.

Balasubramanian, S., Haan, F.L., Szewczyk, A.A., Skop, R.A., 2001. An experimental investigation of the vortex-excited vibrations of pivoted tapered circular cylinders in uniform and shear flow. J. Wind. Eng. Ind. Aerodyn. 89, 757:784. http://dx.doi.org/10.1016/S0167-6105(00)00093-3.

Basu, R.I., Vickery, B.J., 1983. Across-wind vibrations of structures of circular cross-section. Part II. Development of a mathematical model for full-scale application. J. Wind Eng. Ind. Aerodyn. 12, 75–97. http://dx.doi.org/10.1016/0167-6105(83)90081-8.

Blevins, R.D., 2001. Flow-Induced Vibration, second ed Krieger Publ. Company, Malabar FL.

Brusco, S., Buresti, G., Lo, Y.-L., Piccardo, G., 2022b. Constant-frequency time cells in the vortex-shedding phenomenon from a square cylinder in accelerating flows. J. Wind Eng. Ind. Aerodyn. 230, 105182. http://dx.doi.org/10.1016/j.jweia.2022.105182.

Brusco, S., Buresti, G., Piccardo, G., 2022a. Thunderstorm-induced mean wind velocities and accelerations through the continuous wavelet transform. J. Wind Eng. Ind. Aerodyn. 221, 104886. http://dx.doi.org/10.1016/j.jweia.2021.104886.

Buresti, G., 1998. Vortex shedding from bluff bodies. In: Riera, J.D., Davenport, A.G. (Eds.), Wind Effects on Buildings and Structures. Balkema, Rotterdam, pp. 61–95.

Buresti, G., Lombardi, G., Bellazzini, J., 2004. On the analysis of fluctuating velocity signals through methods based on the wavelet and Hilbert transforms. Chaos Solitons Fractals 20, 149–158. http://dx.doi.org/10.1016/S0960-0779(03)00438-7.

Chen, Z., Fu, X., Xu, Y., Li, C.Y., Kim, B., Tse, K.T., 2021a. A perspective on the aerodynamics and aeroelasticity of tapering: Partial reattachment. J. Wind Eng. Ind. Aerodyn. 212, 104590. http://dx.doi.org/10.1016/j.jweia.2021.104590.

Chen, Z., Huang, H.X., Xu, Y., Tse, K.T., Kim, B., Wang, Y., 2021b. Unsteady aerodynamics on a tapered prism under forced excitation. Eng. Struct. 240, 112387. http://dx.doi.org/10.1016/j.engstruct.2021.112387.

ESDU 80025, 1986. Mean forces, pressures and flow field velocities for circular cylindrical structures: single cylinder with two-dimensional flow.

ESDU 81017a, 1987. Mean forces, pressures and moments for circular cylindrical structures: finite-length cylinders in uniform and shear flow.

ESDU 96030, 1998. Response of structures to vortex shedding; structures of circular or polygonal cross section.

Facchinetti, M.L., de Langre, E., Biolley, F., 2002. Vortex shedding modeling using diffusive van der Pol oscillators. C. R. Mec. 330, 451–456. http://dx.doi.org/10.1016/S1631-0721(02)01492-4.

Feng, C.C., 1968. The Measurement of Vortex-Induced Effects in a Flow Past Stationary and Oscillating Circular and D-Section Cylinders (MSc th). Univ British Columbia.

Gaster, M., 1971. Vortex shedding from circular cylinders at low Reynolds numbers. J. Fluid Mech. 46 (4), 749–756. http://dx.doi.org/10.1017/S002211207100082X.

Griffin, O.M., 1985. Vortex shedding from bluff bodies in a shear flow. ASME J. Fluids Eng. 107, 298:306. http://dx.doi.org/10.1115/1.3242481.

Guo, Y., Kareem, A., 2016. Non-stationary frequency domain system identification using time-frequency representations. Mech. Syst. Signal Process. 72–73, 712–726. http://dx.doi.org/10.1016/j.ymssp.2015.10.031.

Guo, K., Yang, Q., Liu, M., Li, B., 2021. Aerodynamic damping model for vortex-induced vibration of suspended circular cylinder in uniform flow. J. Wind. Eng. Ind. Aerodyn. 209, 104497. http://dx.doi.org/10.1016/j.jweia.2020.104497.

Hsiao, F.-B., Chiang, C.-H., 1998. Experimental study of cellular shedding vortices behind a tapered circular cylinder. Exp. Therm. Fluid Sci. 17, 179–188. http://dx.doi.org/10.1016/S0894-1777(98)00004-1.

Huang, C.S., Su, W.C., 2007. Identification of modal parameters of a time invariant linear system by continuous wavelet transformation. Mech. Syst. Signal Process. 21, 1642–1664. http://dx.doi.org/10.1016/j.ymssp.2006.07.011.

Kaja, K., Zhao, M., Xiang, Y., Cheng, L., 2016. Three-dimensional numerical simulations of vortex-induced vibrations of tapered circular cylinders. Appl. Ocean Res. 60, 1–11. http://dx.doi.org/10.1016/j.apor.2016.08.004.

Kay, N.J., O, N.L., Richards, P.J., Sharma, R.N., 2020. Characteristics of fluctuating pressure measurement systems utilizing lengths of 2D-printed tubing. J. Wind Eng. Ind. Aerodyn. 199, 104121. http://dx.doi.org/10.1016/j.jweia.2020.104121.

Kwok, K.C.S., Melbourne, W.H., 1981. Wind-induced lock-in excitation of tall structures. J. Struct. Div. – ASCE 107, 57–72. http://dx.doi.org/10.1061/JSDEAG.0005637.

Laneville, A., 1990. Turbulence and blockage effects on two dimensional rectangular cylinders. J. Wind Eng. Ind. Aerodyn. 33 (1–2), 11–20. http://dx.doi.org/10.1016/0167-6105(90)90016-6.

Lupi, F., Höffer, R., Niemann, H.-J., 2021. Aerodynamic damping in vortex resonance from aeroelastic wind tunnel tests on a stack. J. Wind Eng. Ind. Aerodyn. 208, 104438. http://dx.doi.org/10.1016/j.jweia.2020.104438.

Mariotti, A., 2018. Axisymmetric bodies with fixed and free separation: Base-pressure and near-wake fluctuations. J. Wind Eng. Ind. Aerodyn. 176, 21–31. http://dx.doi.org/10.1016/j.jweia.2018.03.003.

Mariotti, A., Buresti, G., 2013. Experimental investigation on the influence of boundary layer thickness on the base pressure and near-wake flow features of an axisymmetric blunt-based body. Exp. Fluids 54 (11), 1612. http://dx.doi.org/10.1007/s00348-013-1612-5.

Mariotti, A., Buresti, G., Gaggini, G., Salvetti, M.V., 2017. Separation control and drag reduction for boat-tailed axisymmetric bodies through contoured transverse grooves. J. Fluid Mech. 832, 514–549. http://dx.doi.org/10.1017/jfm.2017.676.

Maull, D.J., Young, R.A., 1973. Vortex shedding from bluff bodies in a shear flow. J. Fluid Mech. 60 (2), 401–409. http://dx.doi.org/10.1017/S0022112073000236.

Onorato, M., Salvetti, M.V., Buresti, G., Petagna, P., 1997. Application of a wavelet cross-correlation analysis to DNS velocity signals. Eur. J. Mech. B-Fluid 16, 575–597.

Pagnini, L.C., Piccardo, G., 2017. A generalized gust factor technique for evaluating the wind-induced response of aeroelastic structures sensitive to vortex-induced vibrations. J. Fluids Struct. 70, 181–200. http://dx.doi.org/10.1016/j.jfluidstructs.2017.01.017.

Pagnini, L.C., Piccardo, G., Solari, G., 2020. VIV regimes and simplified solutions by the spectral model description. J. Wind. Eng. Aerodyn. 198, 104100. http://dx.doi.org/10.1016/j.jweia.2020.104100.

Papangelou, A., 1992. Vortex shedding from slender cones at low Reynolds numbers. J. Fluid Mech. 242, 299–321. http://dx.doi.org/10.1017/S0022112092002386.

Peterka, J.A., Meroney, R.N., Kothari, K.M., 1985. Wind flow patterns about buildings. J. Wind. Eng. Aerodyn. 21 (1), 21–38. http://dx.doi.org/10.1016/0167-6105(85)90031-5.

Piccirillo, P., Van Atta, C., 1997. The evolution of a uniformly sheared thermally stratified turbulent flow. J. Fluid Mech. 334, 61–86. http://dx.doi.org/10.1017/S002211209600434X.

Sarpkaya, T., 2004. A critical review of the intrinsic nature of vortex-induced vibrations. J. Fluids Struct. 19, 389–447. http://dx.doi.org/10.1016/j.jfluidstructs.2004.02.005.

Scruton, C., 1956. Note on the Aerodynamic Stability of Truncated Circular Cones and Tapered Stacks. Unpublished Report NPL/Aero/305, Teddington, UK.

Scruton, C., 1963. On the wind-excited oscillations of stacks, towers and masts. In: Proceedings of the International Conference on the Wind Effects on Buildings and Structures. Teddington, UK, pp. 798–832.

Scruton, C., Flint, A.R., 1964. Wind-excited oscillations of structures. Proc. Inst. Civ. Eng. 27 (4), 673–702. http://dx.doi.org/10.1680/iicep.1964.10179.

Solari, G., 1985. Mathematical model to predict 3-D wind loading on buildings. J. Eng. Mech. 111 (2), 254–276. http://dx.doi.org/10.1061/(ASCE)0733-9399(1985)111:2(254).

Solari, G., 2019. Wind Science and Engineering. Springer Nature, Switzerland.

Solìs, M., Albaga, M., Galvìn, P., 2013. Continuous wavelet analysis of mode shapes differences for damage detection. Mech. Syst. Signal Process. 40, 645–666. http://dx.doi.org/10.1016/j.ymssp.2013.06.006.

Techet, A.H., Hover, F.S., Triantafyllou, M.S., 1998. Vortical patterns behind a tapered cylinder oscillating transversely to a uniform flow. J. Fluid Mech. 363, 79–96. http://dx.doi.org/10.1017/S0022112098001104.

Vandiver, J.K., 2012. Damping parameters for flow-induced vibration. J. Fluids Struct. 35, 105–119. http://dx.doi.org/10.1016/j.jfluidstructs.2012.07.002.

Vickery, B.J., 1981. Across-wind buffeting in a group of four in-line model chimneys. J. Wind Eng. Ind. Aerodyn. 8, 177–193. http://dx.doi.org/10.1016/0167-6105(81)90017-9.

Vickery, B.J., Basu, R.I., 1983. Across-wind vibrations of structures of circular cross-section. Part I. Development of a mathematical model for two-dimensional conditions. J. Wind Eng. Ind. Aerodyn. 12, 49–73. http://dx.doi.org/10.1016/0167-6105(83)90080-6.

Vickery, B.J., Clark, A.W., 1972. Lift or across-wind response of tapered stacks. J. Struct. Div. ASCE 98 (1), 1–20. http://dx.doi.org/10.1061/JSDEAG.0003103.

Walshe, D.E.J., 1972. Wind-Excited Oscillations of Structures. National Physical Laboratory, HMSO, London.

Wang, J., Kopp, G.A., 2021. Gust effect factors for windward walls of rigid buildings with various aspect ratios. J. Wind Eng. Ind. Aerodyn. 221, 104603. http://dx.doi.org/10.1016/j.jweia.2021.104603.

Williamson, C.H.K., Govarhan, R., 2004. Vortex-induced vibration. Ann. Rev. Fluid Mech. 36, 413–455. http://dx.doi.org/10.1146/annurev.fluid.36.050802.122128.

Williamson, C.H.K., Roshko, A., 1988. Vortex formation in the wake of an oscillating cylinder. J. Fluid Struct. 2, 355–381. http://dx.doi.org/10.1016/S0889-9746(88)90058-8.

Wooton, L.R., 1969. The oscillations of large circular stacks in wind. Proc. Inst. Civil Eng. 43, 573–598. http://dx.doi.org/10.1680/iicep.1969.7314.

Zdravkovich, M.M., 1982. Scruton number: a proposal. J. Wind. Eng. Ind. Aerodyn. 10, 263–265. http://dx.doi.org/10.1016/0167-6105(82)90001-0.

Zeinoddini, M., Tamimi, V., Seif, M.S., 2013. Stream-wise and cross-flow vortex induced vibrations of single tapered circular cylinders: An experimental study. Appl. Ocean Res. 42, 124–135. http://dx.doi.org/10.1016/j.apor.2013.05.005.

Zuo, D., Letchford, C.W., 2010. Wind-induced vibration of a traffic-signal-support structure with cantilevered tapered circular mast arm. Eng. Struct. 32, 3171–3179. http://dx.doi.org/10.1016/j.engstruct.2010.06.005.